Ocean Engineering 308 (2024) 118311

Contents lists available at ScienceDirect

Ocean Engineering

journal homepage: www.elsevier.com/locate/oceaneng

Research paper

Benchmarking of spectral methods for fatigue assessment of mooring systems and dynamic cables in offshore renewable energy technologies

Eguzkiñe Martinez-Puente [a,*], Ander Zarketa-Astigarraga [a], Manex Martinez-Agirre [a], Alaitz Zabala [b], Jon Ander Esnaola [c], Miguel Muñiz-Calvente [d], Iñigo Llavori [b,c], Markel Penalba [a,e]

[a] Fluid Mechanics Department, Mondragon University, Loramendi 4, 20500 Arrasate, Spain
[b] Surface Technologies, Mondragon University, Loramendi 4, 20500 Arrasate, Spain
[c] Structural Mechanics and Design, Mondragon University, Loramendi 4, 20500 Arrasate, Spain
[d] Department of Construction and Manufacturing Engineering, University of Oviedo, Gijón 33203, Spain
[e] Ikerbasque, Basque Foundation for Science, Euskadi Plaza 5, 48011 Bilbao, Spain

ARTICLE INFO

Dataset link: https://github.com/MGEP-Fluidos/ORE-Structural-Integrity.git

Keywords:
Offshore renewable energy
Mooring systems
Fatigue modelling
Frequency-domain
Rainflow-counting
Damage

ABSTRACT

Fatigue life estimation methods based on time-domain and rainflow counting techniques are widely recognised and accepted for their reliability. However, applying them in scenarios involving random loads with multiple large-scale time series becomes impractical due to high computational costs. This challenge is particularly significant for offshore renewable energy systems. Therefore, it is essential to employ more efficient frequency domain fatigue life calculation models. This study critically evaluates various spectral fatigue assessment methods for estimating damage caused by stress loads in the offshore environment. In this research, 25 spectral methods are analysed and compared using synthetic tension signals. The evaluation criteria include the results' reliability and ease of implementation, leading to the development of a scoring scheme as a systematic and straightforward ranking method. The results reveal that the Tovo–Benasciutti method excels in accurately estimating rainflow damage in bimodal processes, closely followed by the empirical $\alpha_{0.75}$, Han–Ma, Low, Modified Tovo–Benasciutti, Dirlik, and Jun–Park models. Other popular methods, such as the Narrow-band and Wirsching–Light methods, yielded poor results, and their use is discouraged. Furthermore, the spectral methods analysed in the benchmarking study have been implemented in Python, and the code has been released as open source.

1. Introduction

Offshore Renewable Energy (ORE) technologies encompass a range of clean energy solutions, each with significant potential but at different stages of maturity. Offshore wind, with an installed capacity of 34 GW (2020 data) and the potential to reach 382 GW by 2030 and 2002 GW by 2050 is the most mature (IRENA, 2021). Ocean energy holds an abundance of untapped resource potential divided into different technologies. Tidal energy, with a potential of 1200 TWh (IRENA, 2020) is the most mature of the ocean energy technologies, while wave energy is recognised as the largest untapped ocean energy source, with an estimated annual production potential of 29,500 TWh (IRENA, 2020). Lastly, floating photovoltaic (fPV) is expected to be important among ORE technologies, for which a study by the National Renewable Energy Laboratory in the United States predicts the potential to install 7.8 TW with an annual power generation capacity of 10,600 TWh (IRENA, 2021). Despite some of these technologies being in the early stages of development (Astariz and Iglesias, 2015; Leijon et al., 2006), numerous studies highlight the potential for substantial cost reductions through further industrialisation (Gondal, 2019; IRENA, 2021; Martinez and Iglesias, 2022; Sykes et al., 2023).

In the case of wave energy converters (WECs), a recent comprehensive review of economic aspects estimated that 10% of the cost of WECs is due to the mooring system cost and another 10% of the capital expenditure is due to the cost of the dynamic power cables (Astariz and Iglesias, 2015). Material costs aside, expenses incurred in the installation (Astariz and Iglesias, 2015) were estimated at 50,000 €/day for the mooring installation (Couñago Lorenzo et al., 2010) and 2.07 €/m for the cable installation (Farley, 2013). Similar figures for moorings and dynamic cables were also estimated in other ORE technologies, such as floating offshore wind (Catapult, 2023) and tidal (Previsic and Chozas, 2015). Therefore, the relevance of moorings and dynamic cables has been demonstrated in economic terms.

* Corresponding author.
E-mail address: emartinezp@mondragon.edu (E. Martinez-Puente).

https://doi.org/10.1016/j.oceaneng.2024.118311
Received 16 January 2024; Received in revised form 20 May 2024; Accepted 27 May 2024
Available online 7 June 2024

Nomenclature

Symbols

α_{k}	k-th bandwidth parameter, $\alpha_n = \frac{\lambda_n}{\sqrt{\lambda_0 \lambda_{2n}}}$
β	generalised spectral bandwidth
δ_2	Vanmarcke's bandwidth parameter
ϵ	spectral width parameter
γ	ratio between the absolute maximum value of the process and S_{u}
γ_3	skewness
γ_4	kurtosis
λ_{n}	n-th spectral moment, $\lambda_{\mathrm{n}} = \int_0^\infty \omega^n W_x(\omega)\,\mathrm{d}\omega$
$\Gamma(.)$	Euler gamma function
μ_{k}	k-th special bandwidth parameter
ν_{p}	expected peak frequency
ν_0^+	mean zero up-crossing frequency
$\Phi(.)$	standard normal distribution function
Ψ	high- and low-frequency offset phase
ρ	damage correction factor
σ	standard deviation
σ^2	variance
θ	phase angle
ε	strain
$\varepsilon(s_{\mathrm{LF}}, \theta)$	discrepancy between the high frequency and small cycle stress amplitudes
B	spacing between LF and HF components
b	weighting coefficient
C	fatigue strength coefficient
D	absolute amount of damage
d	damage rate or damage per unit of time
d_{diff}	relative damage difference
d_{norm}	normalised damage
k	fatigue exponent
$L(\sigma^2_{\mathrm{HF}}, B, k)$	low frequency damage ratio
m	mean stress
$M_{\mathrm{RR}}(\mathrm{n})$	n-th order moments of rainflow stress range
M_k	rainflow stress range distribution moment
n	number of cycles
N	number of cycles to failure
$p_{\mathrm{a}}(s)$	cycle amplitude Probability Density Function
Q_c	damage correction factor
r	stress range
r_e	Goodman equivalent stress range
s	stress amplitude
S_{u}	ultimate tensile strength
T	total life
w	weighting coefficient
$X(t), Y(t)$	random processes

Abbreviations

A75	The empirical a0.75 method
API	American Petroleum Institute
BM	Bands method
DK	Dirlik method
DNB	Dual narrow-band method
DNV	Det Norske Veritas
EA	Line Stiffness
EI	Error Index
FC	Fu–Cebon method
FD	Frequency-domain
FIP	Fatigue Indicator Parameter
FLS	Fatigue Limit State
FOWT	Floating Offshore Wind Turbine
fPV	Floating Photovoltaic
GM	Gao–Moan method
GZ	Gao–Zheng method
HF	High Frequency
HM	Huang–Moan method
HMa	Han–Ma method
IBM	Improved bands method
IQR	Interquartile Range
JM	Jiao–Moan method
JP	Jun–Park method
LB	Lotsberg method
LF	Low Frequency
LOW	Low method
LWB	Low's Bimodal method
MF	Intermediate frequency
MFC	Modified Fu–Cebon method
MTB	Modified Tovo–Benasciutti method
NB	Narrow-band approximation method
OC	Ortiz–Chen method
ORE	Offshore Renewable Energy
PDF	Probability Density Function
PK	Park method
PSD	Power Spectral Density
PZ	Petrucci–Zuccarello method
RC	Range count method
RFC	Rainflow counting
SI	Structural Integrity
SM	Single Moment method
SO	Sakai–Okamura method
SS	Sea State
TB	Tovo–Benasciutti method
TD	Time-domain
ULS	Ultimate Limit State
WEC	Wave Energy Converter
WF	Wave Frequency
WL	Wirsching–Light method
WU	Wu method
ZB	Zhao–Baker method

In addition, the mooring system is designed to keep the ORE systems in station even in the most severe storm conditions (Harris et al., 2004). However, its use is not limited to station-keeping. Mooring systems are sorted into three categories depending on their purpose: (a) passive moorings ensure station-keeping; (b) active moorings can influence the dynamic response and power extraction; and (c) reactive moorings provide reaction forces for wave power extraction (Davidson and Ringwood, 2017). To achieve the intended utility, there are a vast variety of mooring configurations including catenary line (steel chains) and taut-line systems (tendons) with or without clump weights or buoys (Gao and Moan, 2009) (Fig. 1). Each of these configurations can use a different material, such as steel chains, synthetic fibre ropes and steel wire ropes (Ma et al., 2019b).

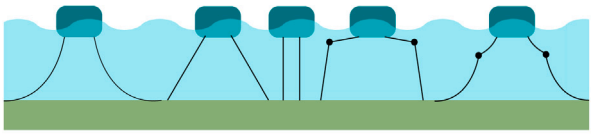

(a) Mooring system configurations

(b) Mooring composition and material

Fig. 1. Mooring system alternatives: (a) Mooring configurations (from left to right: catenary line, taut leg, tension leg, mooring system with buoys, and with clump weights), and (b) mooring composition and materials (from left to right: steel studless chain, steel stud chain, steel wire rope, and synthetic fibre rope).

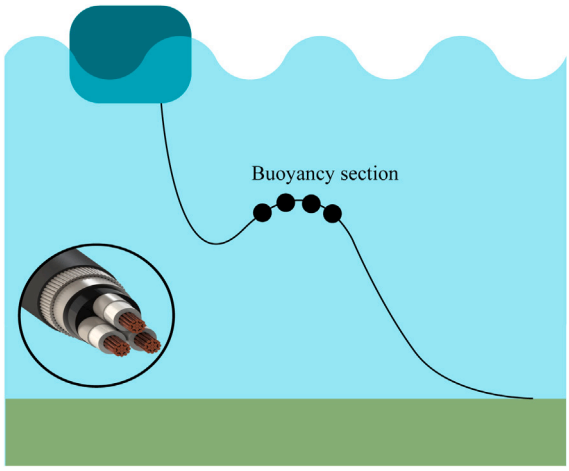

Fig. 2. Dynamic power cable layout and section representation.

Dynamic power cables are also critical subsea transmission components for ORE technologies (Zhao et al., 2021). Given the environmental conditions they are subjected to, their design must be able to withstand extreme dynamic loads and cyclic fatigue damage (Zhao et al., 2021). Dynamic cables, typically arranged in lazy wave configurations (Schnepf et al., 2023; Zhao et al., 2021), consist of a multi-layer design (Fig. 2) that protects the three coaxial core conductors from the environment. Each conductor is covered in an insulation layer that is itself protected by waterproof metal or polymeric sheaths. An armour layer encloses the three cables, protecting them from the marine environment and installation loads. An outer sheath protects the armour from corrosion (Dinmohammadi et al., 2019; Poon et al., 2022).

A reliable method for estimating the structural integrity (SI) of ORE systems enables effective maintenance planning (Giro et al., 2022) and prevents unnecessary overdesign of parts that could limit their performance (Penalba et al., 2021). This assessment typically involves evaluating SI through ultimate limit state (ULS) analysis, addressing failure under extreme loads and fatigue limit state (FLS) analysis. The latter consists of considering cyclic loads that may cause failure below the material's yielding point (Shahroozi et al., 2022). While ULS assessment focuses on critical extreme conditions, fatigue analysis must encompass the entire operational range of the device, which is especially cumbersome in offshore settings where wave conditions vary significantly. This variability necessitates the development of more efficient models to analyse all relevant loading conditions within the operational region.

Typically, FLS assessments are conducted under the assumption of constant stress amplitude (Bergara et al., 2022; Cortabitarte et al., 2023). This approach simplifies the evaluation of material endurance by exposing a specimen to a consistent level of cyclic stress amplitude. However, in the context of ORE applications, where operating conditions often vary, it becomes crucial to consider the dynamic and unpredictable nature of the loads imposed on materials. In such cases, a more realistic representation of fatigue should involve the assessment of variable random fatigue. This involves accounting for the fluctuating stress levels that materials may experience over time due to changing environmental conditions, tidal forces, and other factors inherent to ORE systems (Ma et al., 2019a). These loads are commonly estimated via hydrodynamic simulations, although the literature also suggests machine learning approaches, such as surrogate models (Zhao and Dong, 2021) and, particularly, Artificial Neural Networks (Durodola et al., 2017; Li et al., 2018), for a more efficient random fatigue loading analysis.

Rainflow counting (RFC) (Matsuishi and Endo, 1968), is a well-known time-domain (TD) technique widely recognised for its reliability in estimating fatigue. This holds true provided there is enough data – whether experimental or synthetic – containing essential information about the system's behaviour across its entire operational range. Despite its accuracy, RFC is time-consuming to execute (Ma et al., 2019a).

Frequency-domain (FD) analysis provides a quicker alternative to RFC. Frequency domain analysis entails deriving statistical parameters from the TD response and processing them via different spectral methods (Benasciutti, 2012). However, the damage estimates are dependent on the distributions adopted by each FD approach (Benasciutti, 2012; Slavič et al., 2020).

Despite the benefits of the spectral methods, the vast majority of the fatigue analyses for mooring lines and dynamic cables presented in the literature are based on the computationally more demanding RFC method. For instance, Shahroozi et al. (2022) conducted a fatigue analysis of a point-absorber WEC employing RFC. Similarly, He et al. (2022) performed a fatigue SI assessment of the mooring system for a floating production storage and offloading vessel via RFC and fatigue crack growth models. Barrera et al. (2020) proposed a method for mooring line design against fatigue damage that is calculated by RFC. Lee et al. (2023) focused on stress-based fatigue life estimation for an offshore wind turbine support structure. Sobhaniasl et al. (2020) proposed a procedure using RFC to determine the fatigue life of power cables. Benites-Munoz et al. (2023) also employed RFC for the fatigue assessment of dynamic power cables on a floating testing platform. Okpokparoro and Sriramula (2023) performed a reliability analysis of floating wind turbine dynamic cables, employing RFC to assess fatigue damage. Cevasco et al. (2018) utilised RFC to assess the fatigue of mooring lines for offshore vertical-axis wind turbines. Zhao et al. (2023) performed a mooring system reliability analysis for a floating offshore wind turbine (FOWT) where the fatigue damage was evaluated by means of RFC.

However, offshore standards such as DNV (2021) and API (2005), propose not only the RFC method in TD but also spectral methods as alternatives for fatigue assessment of station-keeping systems for floating offshore structures. More specifically, both DNV and API suggest the use of the Dual narrow-band (DNB) method. Furthermore, Pham et al. (2019) recommend the use of spectral methods, such as the Narrow-band (NB), Tovo–Benasciutti (TB), and Jiao–Moan (JM) methods, to analyse fatigue in mooring lines for FOWTs.

To the best of the authors' knowledge, no benchmark on spectral fatigue modelling approaches exists in the literature within the ORE context. The only studies considering such a large set of spectral models include Muñiz-Calvente et al. (2022), which presented it in a merely descriptive manner, and Zorman et al. (2023), who offered a review of spectral methods focused on vibration fatigue. The current study suggests a critical benchmarking of different spectral methods, aiming

to evaluate them in terms of effectiveness and popularity, and define the most suitable model for assessing fatigue in mooring lines and dynamic cables in ORE systems. For that purpose, a systematic review of a broad set of spectral models available in the literature is carried out, assessing their suitability for ORE applications. The benchmarking suggested in the present paper is based on the catenary mooring lines of the RM3 point absorber (Neary et al., 2014). The damage calculated through the RFC method serves as a reference ground truth for comparing damage estimates obtained through alternative spectral methods. Although the case study in the present paper is limited to WECs and mooring lines, the conclusions on the suitability of the FD approaches assessed here can be extended to other ORE technologies, such as FOWTs and tidal turbines. Furthermore, the spectral methods analysed in the benchmarking study have been implemented in Python and the code has been released as open source.

The paper is structured as follows: Section 2.1 and Section 2.2 describe fatigue assessment methods in the time and frequency domains, respectively. Section 3 presents a classification system of the methods based on their performance. Section 4 introduces the chosen case study, outlining its loading conditions and mooring characteristics. The findings of the case study are presented in Section 5. The paper concludes with final remarks and conclusions in Section 6.

2. Fatigue assessment methodology

A general fatigue damage assessment involves the following steps, as described in the process flowchart in Fig. 3:

1. **Geometry Definition.** The initial step involves defining the geometric parameters and configurations relevant to the structural component under consideration.
2. **Operational Condition Selection.** In this phase the operational conditions, such as loading scenarios and environmental factors, that the structure will be subjected to during its service life are identified.
3. **Material Characterisation.** The fatigue behaviour of the material is analysed to establish the relationship between stress or strain and fatigue life in cycles.

   3.1 **Fatigue Indicator Selection.** A suitable fatigue indicator parameter (FIP) is selected based on the specific material and operational conditions. This parameter gauges the material's reaction to cyclic loading and is usually the stress amplitude, strain amplitude, or a combination of both (Muñiz-Calvente et al., 2022).

4. **Loading History Determination.** The subsequent stage is to determine the loading history corresponding to the chosen FIP based on the data gathered in the previous steps. This history can be acquired from experimental data or numerical simulations.
5. **Damage Evaluation.** Based on the loading history, fatigue analysis is performed either in TD or FD, depending on the available data and analysis requirements.

2.1. Time-domain model: Rainflow counting

In TD fatigue analysis, the loading history is segmented into stress ranges with their corresponding cycle counts. The rainflow counting method, introduced by Matsuishi and Endo (1968), is widely employed to analyse complex random loadings. Inspired by the natural path of rain trickling down a pagoda roof, the loading history is rotated 90° clockwise to replicate this pattern, as illustrated in Fig. 4. According to RFC, the rain flow starts from a peak or valley and drips down until:

(a) It reaches a point opposite a larger maximum (or smaller minimum) value. For instance, as shown in Fig. 4, the flow dripping from BC ends when it meets the flow falling from D, as the latter starts from a larger maximum value.

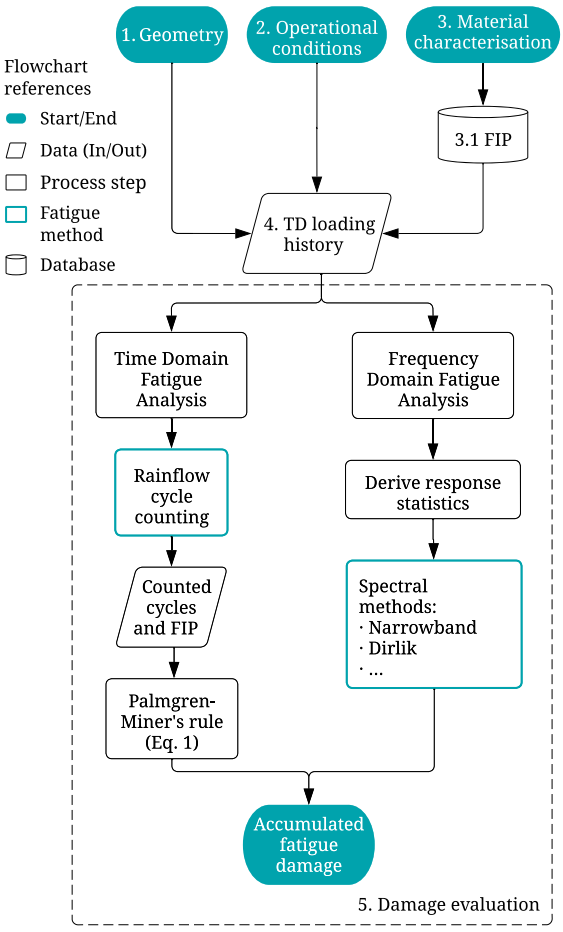

Fig. 3. Fatigue evaluation flowchart.

(b) It intersects with a preceding flow falling from above. For example, in Fig. 4, the flow dripping from C ends when it meets with the one falling from AB, as the latter is descending from a preceding point above.

(c) It descends below the roof level. As shown in Fig. 4, the flow dripping from A ends when it reaches point D, as there is no larger peak below for it to fall to.

Whenever a rainflow reaches a termination point, indicating a loading reversal or half cycle, it is tallied and given a stress range value, which represents the difference between its starting and ending positions. Half cycles with the same magnitude but opposite directions are then matched to calculate the total number of complete cycles (Lee and Tjhung, 2012).

After identifying the cycles, Miner's rule (Miner, 1945) is employed to estimate the accumulated damage resulting from these cycles. Miner's rule is based on the principle that fatigue damage increases linearly with the number of cycles experienced by the material. Each cycle is assigned a damage value based on its amplitude and the endurance limit obtained from the corresponding S–N (stress–life) or ε–N (strain–life) curve for the material. The contribution of damage from each cycle is then aggregated, as follows:

$$D = \sum \frac{n_i}{N_i}, \tag{1}$$

where, n_i is the number of cycles within the magnitude range interval i and N_i is the number of cycles to failure at magnitude range i.

If the cumulative damage surpasses unity, it indicates that the material is likely to fail due to fatigue.

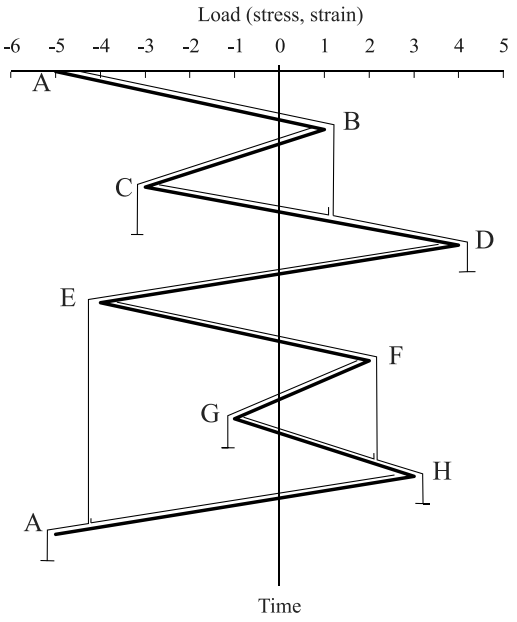

Fig. 4. Rainflow cycle counting of the loading history, (Lee and Tjhung, 2012).

2.2. Spectral methods

The various spectral methods present a computationally efficient option by examining the loading spectrum, which collects all the important statistical characteristics of the load history. Given that the RFC method is widely acknowledged for its accuracy, these spectral approaches attempt to depict the statistical distribution of rainflow cycles (Benasciutti, 2012).

Considering that the increase in damage relies on the constant-amplitude fatigue properties described by the S–N curve, Miner's equation can be reformulated as follows:

$$D = \sum \frac{s_i^k}{C}, \tag{2}$$

where, s_i is the stress amplitude of the i-th counted cycle, k is the S–N curve slope and C is the fatigue strength.

In FD analyses, damage is commonly discussed in terms of the damage rate, or damage per unit of time:

$$d = \frac{D}{T}, \tag{3}$$

where, D is the absolute amount of damage and T is the total lifetime.

The damage intensity can be deduced by integrating the probability density function (PDF) of cycle amplitudes over the range of stress cycle amplitudes (Benasciutti, 2012; Slavič et al., 2020):

$$d = \nu_p C^{-1} \int_0^{+\infty} s^k p_a(s) \mathrm{d}s, \tag{4}$$

where, ν_p is the expected peak frequency, and $p_a(s)$ is the cycle amplitude PDF.

The estimation of the cycle amplitude probability, which is typically determined implicitly through spectral moment methods, relies on the assumption that the process and its power spectral density (PSD) follow a Gaussian distribution (Slavič et al., 2020).

Obtaining an accurate expression of the cycle distribution and establishing a connection with the spectral density of the random process would constitute a more comprehensive approach. Nevertheless, due to the complex algorithm utilised in rainflow counting, determining the relationship between the cycle distribution and the TD (or FD) characteristics of the process is exceedingly challenging. As a result, to date, the true expression of the distribution remains unknown for wide-band processes (Benasciutti, 2012).

To tackle this issue, some methods either rely on theoretical considerations or resort to approximation techniques involving fitting procedures applied to numerous simulation outcomes (Benasciutti, 2012).

In the most recent review of spectral methods, Zorman et al. (2023) organised the broadband spectral models into four groups according to the approach used for the damage estimation (Fig. 5):

(a) **Narrow-band correction factor:** This concept involves incorporating a correction factor into the narrow-band fatigue-damage model, allowing it to be applied to broadband processes.
(b) **Rainflow approximation:** In this group, the methods are divided into PDF or moment approximations. In the former, the PDF of rainflow stress cycles is approximated, while in the latter, the rainflow stress range distribution moment is approximated based on the PSD of the loading response.
(c) **Combined fatigue damage – cycle type damage combination:** Broadband random processes, such as multimodal processes, consist of multiple well-separated narrow-band contributions. The spectral methods in this group focus on estimating damage for each cycle type independently and then summing up the damage contributions from all cycle categories to obtain the combined fatigue damage.
(d) **Combined fatigue damage – narrow-band damage combination:** The combined fatigue damage is expressed explicitly in terms of a nonlinear combination of individual damages. To achieve this, the broadband stress spectrum is decomposed into a collection of narrow-band spectral contributions.

Table 1 presents a summary of a critical comparative review of the spectral methods found in the literature and presented in this section. This review explores various aspects, such as the popularity and practical applicability of each method, assessed through citation rates and industry recommendations. Additionally, the stress process types addressed by these methods, categorised as broadband, bimodal, or trimodal, have been systematically examined. The investigation further distinguishes whether the methods rely on empirical or theoretical foundations. Moreover, the state-of-the-art review delves into the specific properties of the stress processes considered by each method, including the utilisation of spectral moments, the incorporation of bandwidth parameters, and other defining characteristics. This analysis provides valuable insights into the diverse approaches employed in the literature.

2.2.1. Narrow-band method

In the context of strictly narrow-band Gaussian processes, the cycle amplitude distribution aligns with the peak amplitude distribution, specifically a Rayleigh distribution. In this scenario, the intensity of the counted cycles can be regarded as the mean zero up-crossing frequency, ν_0^+. Eq. (4) then assumes the following form:

$$d_{NB} = \nu_0^+ C^{-1} \left(\sqrt{2\lambda_0}\right)^k \Gamma\left(1 + \frac{k}{2}\right), \tag{5}$$

where λ_0 is the zeroth spectral moment and $\Gamma(\cdot)$ is the Euler gamma function (Benasciutti, 2012; Miles, 1954).

2.2.2. Wirsching–Light method

In the instance of broad-band signals, the narrow-band approximation method is widely known to yield overestimated results (Rychlik, 1993). Wirsching and Light (1980) addressed this limitation by proposing an empirical correction factor derived from rainflow analysis of simulated broad-band spectra, which is then applied to adjust the narrow-band approximation damage, calculated via Eq. (5).

This correction factor is assumed to be dependent on fatigue curve parameters and the α_2 bandwidth parameter (Benasciutti, 2012).

$$\rho_{WL} = a(k) + [1 - a(k)](1 - \epsilon)^{b(k)}, \tag{6}$$

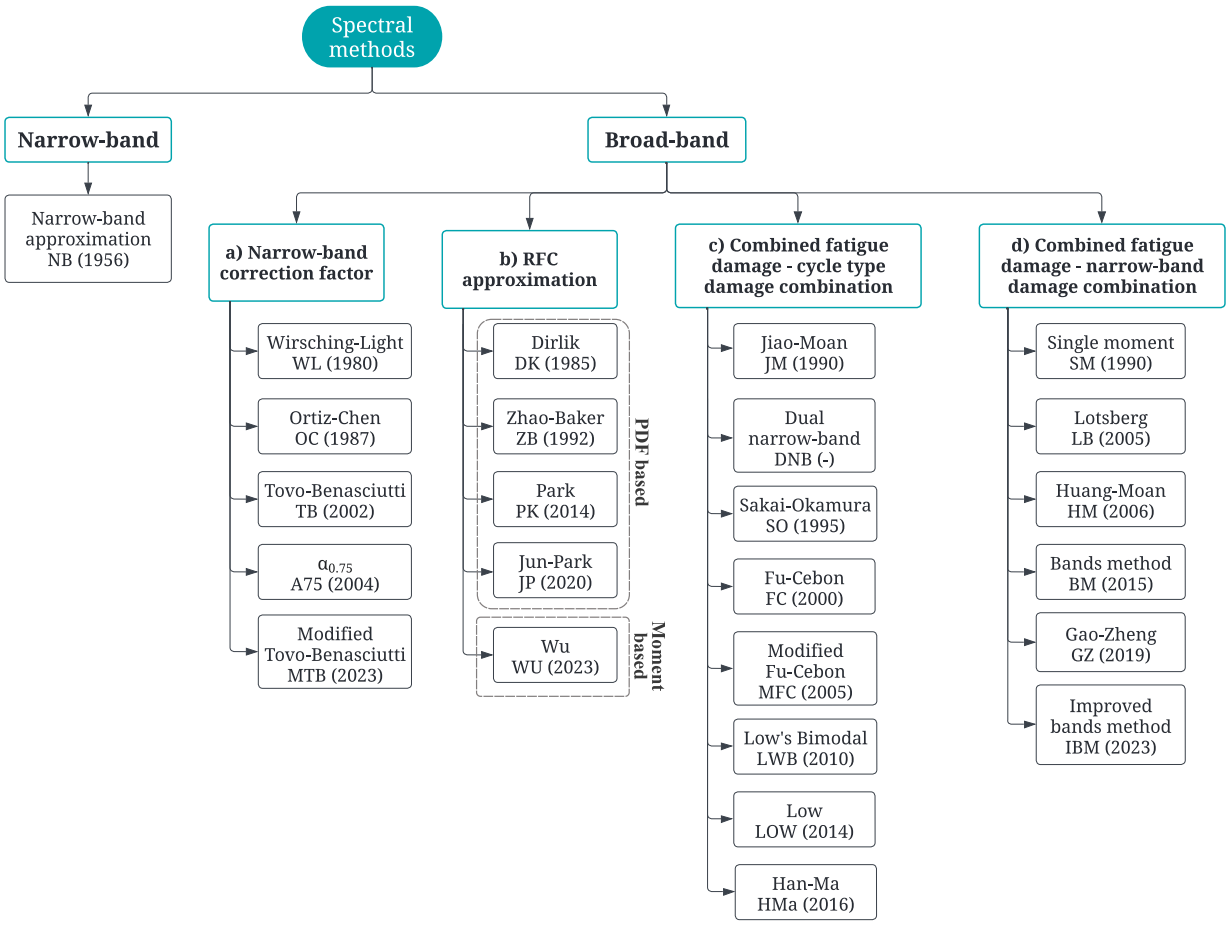

Fig. 5. Classification of spectral methods based on Zorman et al. (2023) with new added methods.

where, ϵ is a spectral width parameter:

$$\epsilon = \sqrt{1 - \alpha_2^2}, \tag{7}$$

and $a(k)$ and $b(k)$ are best fitting parameters dependent on the S–N curve slope k:

$$a(k) = 0.926 - 0.033k, \qquad b(k) = 1.587k - 2.323. \tag{8}$$

2.2.3. Ortiz–Chen method

Ortiz and Chen (1987) developed a correction factor for the narrow-band damage that introduced the generalised spectral bandwidth, β (Zorman et al., 2023):

$$\rho_{\mathrm{OC}} = \frac{\beta^k}{\alpha_2}, \tag{9}$$

where β is dependent on the S–N curve's fatigue-strength exponent k (Zorman et al., 2023):

$$\beta = \sqrt{\frac{\lambda_2 \lambda_{2/k}}{\lambda_0 \lambda_{2/k+2}}}. \tag{10}$$

2.2.4. Tovo–Benasciutti method

The method presented by Benasciutti and Tovo (2005), Tovo (2002) is based on Rychlik (1993)'s findings about the existence of upper and lower damage bounds limiting the expected rainflow damage rate:

$$d_{\mathrm{RC}} \leq d_{\mathrm{RFC}} \leq d^+ = d_{\mathrm{NB}}. \tag{11}$$

According to this relation, the lower limiting value coincides with the range count method (RC) in TD, while the upper bound coincides with the narrow-band approximation (see Section 2.2.1) for stationary Gaussian loads.

For the RC damage, no exact analytical expression is known at present, so the approximate result proposed by Madsen et al. (2006) can be adopted:

$$d_{\mathrm{RC}} \cong \nu_{\mathrm{p}} C^{-1} (\sqrt{2\lambda_0}\alpha_2)^k \Gamma\left(1 + \frac{k}{2}\right) = \alpha_2^{k-1} d_{\mathrm{NB}}. \tag{12}$$

The proposed solution is a linear combination of the upper and lower limits:

$$d_{\mathrm{TB}} = \left[b + (1-b)\alpha_2^{k-1}\right] d_{\mathrm{NB}}, \tag{13}$$

where b is a weighting factor dependent on the PSD through bandwidth parameters α_1 and α_2:

$$b = \frac{(\alpha_1 - \alpha_2)}{(\alpha_2 - 1)^2} \times \left[1.112(1 + \alpha_1\alpha_2 - (\alpha_1 + \alpha_2))e^{2.11\alpha_2} + (\alpha_1 - \alpha_2)\right]. \tag{14}$$

2.2.5. The empirical $\alpha_{0.75}$ method

In light of Lutes et al. (1984)'s findings suggesting a link between rainflow damage and $\alpha_{0.75}$, Benasciutti and Tovo (2004) introduced a correction factor for the narrow-band damage, estimated following Eq. (5). They argued, on a purely empirical basis, that the correction factor is only a function of $\alpha_{0.75}$, and independent of the S–N slope parameter, k:

$$\rho_{0.75} = \alpha_{0.75}^2. \tag{15}$$

This correction factor, as formulated, demonstrated a substantial alignment with simulation data (Benasciutti, 2012; Benasciutti and Tovo, 2004).

Table 1
Literature review summary table, showing the main characteristics of the frequency domain methods.

Method	Stress process	Approach		Spectral moments	Bandwidth parameters	Amplitude distribution	Large cycles		Small cycles	
		Other	Cor. factor				Cycle frequency	Amplitude distribution	Cycle frequency	Amplitude distribution
NB	Narrow-band Gaussian			λ_0		Ray				
WL	Broad-band Gaussian	Empiric	×	λ_0	×					
OC			×	λ_0, λ_2, $\lambda_{2/k}$, $\lambda_{2/k+2}$	×					
TB	Broad-band Gaussian		×	λ_0	×	Ray., RC				
A75	Broad-band Gaussian	Empiric	×	λ_0	×					
MTB	Broad-band non-Gaussian		×	λ_0	×	Ray., RC				
DK	Broad-band Gaussian	Empiric PDF approx.		λ_0, λ_1, λ_2, λ_4	×	Exp., two Ray.				
ZB	Broad-band Gaussian	Empiric PDF approx.		λ_0	×	Weib., Ray.				
PK	Broad-band Gaussian, Bimodal	Empiric PDF approx.		λ_0	×	Ray., std Ray., half-Gaussian				
JP	Broad-band Gaussian	Empiric PDF approx.		λ_0	×	Exp., Ray., std Ray., half-Gaussian				
WU	Broad-band	RFC moment approx.		λ_0	×					
JM	Well-separated bimodal	Cycle type combination	×	λ_0	×		$\nu_{0,P}$	two Ray.	$\nu_{0,HF}$	Ray.
SO	Gaussian bimodal	Cycle type combination		λ_0, λ_2			$\nu_{0,LF}$	Ray.	$\nu_{0,HF}$	Ray.
FC	Gaussian bimodal	Cycle type combination		λ_0			$\nu_{0,LF}$	Two Ray.	$\nu_{0,HF} - \nu_{0,LF}$	Ray.
MFC	Gaussian bimodal	Cycle type combination		λ_0			$\nu_{0,P}$	two Ray.	$\nu_{0,HF} - \nu_{0,P}$	Ray.
LWB	Gaussian bimodal	Cycle type combination		λ_0			$\nu_{0,LF}$	Uni., two Ray.	$\nu_{0,HF} - \nu_{0,LF}$	Uni., two Ray.
LOW	Gaussian bimodal	Cycle type combination	×	λ_0						
HMa	Gaussian bimodal	Cycle type combination		λ_0			$\nu_{0,LF}$	Ray.	$\nu_{0,HF}$	Ray.
SM	Gaussian bimodal	NB combination		$\lambda_{2/k}$						
LB	Gaussian bimodal	NB combination		λ_0						
HM	Gaussian bimodal	NB combination		λ_0						
BM	Broad-band	NB combination		λ_0						
GZ	Gaussian bimodal	NB combination		$\lambda_{2/k}$						
IBM	Broad-band	NB combination		λ_0						
PZ	Broad-band	Mean stress correction		λ_0	×					

Note: "Ray" denotes Rayleigh, "Weib" denotes Weibull, "Exp" denotes Exponential, "Uni" denotes Uniform, and "Norm" denotes Normal.

2.2.6. Modified Tovo–Benasciutti method

Yuan and Sun (2023) extended the TB method for non-Gaussian random processes by proposing a refined formulation of the weighting factor b in Eq. (13). The proposed weighting coefficient incorporates bandwidth parameters α_1 and α_2, the slope of the S–N curve, and the skewness, γ_3 and kurtosis, γ_4 of non-Gaussian processes:

$$b = \frac{(\alpha_1 - \alpha_2)(P_1 + P_2\alpha_2 - P_3\alpha_1\alpha_2)}{(1 - P_4\alpha_2)^2}(P_5\gamma_3^2 + P_6\gamma_4^2 + P_7\gamma_4 + P_8\gamma_3^2\gamma_4 + 1 - 9P_6 - 3P_7), \tag{16}$$

where P_i are coefficients dependent on the S–N curve slope k. These coefficients were approximated through best-fitting procedures on non-Gaussian processes obtained by the transformation of five standard spectra of different shapes (Yuan and Sun, 2023).

2.2.7. Dirlik method

Dirlik (1985) introduced an entirely empirical formula for approximating the rainflow amplitude distribution. This method was derived from extensive numerical simulations, lacking support from any theoretical framework (Benasciutti, 2012).

Through an analysis of density functions derived from his simulations, Dirlik observed that rainflow-range densities exhibited an exponential variation near the origin, with mid-range values following a Rayleigh function. Moreover, Dirlik identified the presence of a high-range standard Rayleigh distribution, which explained the delay in the rainflow-range densities reaching zero. Consequently, the proposed formulation is a combination of these three functions:

$$d_{DK} = \frac{\nu_p}{C}\lambda_0^{k/2}\left[G_1 Q^k \Gamma(1+k) + \left(\sqrt{2}\right)^k \Gamma\left(1+\frac{k}{2}\right)\left(G_2|R|^k + G_3\right)\right], \tag{17}$$

where G_1, G_2, G_3, R, Q and x_m are best fitting parameters:

$$x_m = \frac{\lambda_1}{\lambda_0}\left(\frac{\lambda_2}{\lambda_4}\right)^{1/2}, \qquad D_1 = \frac{2(x_m - \alpha_2^2)}{1+\alpha_2^2},$$
$$D_2 = \frac{1 - \alpha_2 - D_1 + D_1^2}{1-R}, \qquad D_3 = 1 - D_1 - D_2, \tag{18}$$
$$Q = \frac{1.25(\alpha_2 - D_3 - D_2 R)}{D_1}, \qquad R = \frac{\alpha_2 - x_m - D_1^2}{1 - \alpha_2 - D_1 + D_1^2}.$$

2.2.8. Zhao–Baker method

Zhao and Baker (1992) introduced a linear combination of a Weibull and a Rayleigh distribution:

$$d_{ZB} = \nu_p \lambda_0^{k/2} C^{-1}\left[w a^{-\frac{k}{b}}\Gamma\left(1+\frac{k}{b}\right) + (a-w)2^{\frac{k}{2}}\Gamma\left(1+\frac{k}{2}\right)\right], \tag{19}$$

where a and b are determined from simulation results and w is the weighting coefficient:

$$a = 8 - 7\alpha_2,$$

$$b = \begin{cases} 1.1, & \text{if } \alpha_2 < 0.9 \\ 1.1 + 9(\alpha_2 - 0.9), & \text{if } \alpha_2 \geq 0.9 \end{cases}$$

$$w = \frac{1-\alpha_2}{1 - \sqrt{\frac{2}{\pi}}\Gamma\left(1+\frac{1}{b}\right)a^{\frac{-1}{b}}}.$$

This method was specifically calibrated for materials with a fatigue-strength exponent falling within the range of $2 \leq k \leq 6$ (Zhao and Baker, 1992).

2.2.9. Park method

Addressing the limitations of the conventional Rayleigh PDF to represent wide-band Gaussian processes, Park et al. (2014) introduced a novel spectral method centred around the RFC PDF approximation. Their approach combines three distinct distributions: a Rayleigh, a standard Rayleigh, and a half-Gaussian:

$$d_{\mathrm{PK}} = \nu_{\mathrm{p}} C^{-1}\left(\sqrt{2\lambda_0}\right)^k \left[\frac{c_{\mathrm{G}}}{\sqrt{\pi}}\sigma_{\mathrm{G}}^k \Gamma\left(\frac{k+1}{2}\right) + c_{\mathrm{R1}}\sigma_{\mathrm{R1}}^k \Gamma\left(1+\frac{k}{2}\right) + c_{\mathrm{R2}}\Gamma\left(1+\frac{k}{2}\right)\right]. \tag{20}$$

Following Dirlik (1985)'s suggestions, the n$^{\mathrm{th}}$-order moments of the rainflow stress range, $M_{\mathrm{RR}}(\mathrm{n})$, were introduced to determine the five unknowns of the distribution:

$$c_{\mathrm{R1}} = \frac{M_{\mathrm{RR}}(2) - M_{\mathrm{RR}}(3)}{\sigma_{\mathrm{R1}}^2(1-\sigma_{\mathrm{R1}})}, \qquad c_{\mathrm{G}} = 1 - c_{\mathrm{R1}} - c_{\mathrm{R2}},$$
$$c_{\mathrm{R2}} = \frac{-\sigma_{\mathrm{R1}} M_{\mathrm{RR}}(2) - M_{\mathrm{RR}}(3)}{1-\sigma_{\mathrm{R1}}}, \qquad \sigma_{\mathrm{R1}} \approx \alpha_2, \tag{21}$$

$$\sigma_{\mathrm{G}} = \frac{\sqrt{\pi}\Gamma(1.5)}{c_{\mathrm{G}}\Gamma(1)}\left(M_{\mathrm{RR}}(1) - c_{\mathrm{R1}}\sigma_{\mathrm{R1}} - c_{\mathrm{R2}}\right).$$

The moments up to the third order are compared and approximated using products of the bandwidth parameters, α_n (Park et al., 2014):

$$M_{\mathrm{RR}}(1) \approx \alpha_2, \qquad M_{\mathrm{RR}}(2) \approx \alpha_{0.95}\alpha_{1.97},$$
$$M_{\mathrm{RR}}(3) \approx \alpha_{0.54}\alpha_{0.93}\alpha_{1.95}. \tag{22}$$

This method was tailored to predict the fatigue behaviour specific to marine engineering applications (Park et al., 2014).

2.2.10. Jun–Park method

Jun and Park (2020) devised a new empirical solution by enhancing Park et al. (2014)'s model with an exponential distribution to represent low-stress areas. In this approach, damage assessment is calculated as a linear combination of an exponential, a half-Gaussian, and two Rayleigh distributions.

The correction factor Q_c is also introduced to fit the model to the RFC distribution. This factor, devised by means of best-fitting procedures, is a 5th-order polynomial dependent on α_1 and α_2.

$$Q_c = 0.903 - 0.28(\alpha_1-\alpha_2) + 4.448(\alpha_1-\alpha_2)^2 - 15.739(\alpha_1-\alpha_2)^3 + 19.57(\alpha_1-\alpha_2)^4 - 8.054(\alpha_1-\alpha_2)^5 + 1.013\alpha_2 - 4.178\alpha_2^2 + 8.362\alpha_2^3 - 7.993\alpha_2^4 + 2.886\alpha_2^5. \tag{23}$$

Thus, the damage assessment equation takes the following form:

$$d_{\mathrm{JP}} = Q_c \nu_{\mathrm{p}} C^{-1}\left(\sqrt{2\lambda_0}\right)^k \left[\frac{D_1}{(\sqrt{\pi})^k}\sigma_{\mathrm{E}}^k \Gamma(1+k) + D_2\sigma_{\mathrm{R}}^k \Gamma\left(1+\frac{k}{2}\right) + D_3\Gamma\left(1+\frac{k}{2}\right) + \frac{D_4}{\sqrt{\pi}}\sigma_{\mathrm{H}}^k \Gamma\left(\frac{1+k}{2}\right)\right]. \tag{24}$$

Inspired by Park et al. (2014)'s methodology, the moments of rainflow stress range, $M_{\mathrm{RR}}(\mathrm{n})$, are employed to find the distribution unknowns:

$$D_1 = \frac{2(\alpha_1\alpha_2 - \alpha_2^2)}{1+\alpha_2^2}, \tag{25}$$
$$D_2 = \frac{M_{\mathrm{RR}}(2) - M_{\mathrm{RR}}(3)}{\sigma_{\mathrm{R}}^2(1-\sigma_{\mathrm{R}})}, \tag{26}$$
$$D_3 = \frac{-\sigma_{\mathrm{R}} M_{\mathrm{RR}}(2) - M_{\mathrm{RR}}(3)}{(1-\sigma_{\mathrm{R}})}, \tag{27}$$
$$D_4 = 1 - D_1 - D_2 - D_3, \tag{28}$$
$$\sigma_{\mathrm{R}} = \alpha_2, \tag{29}$$
$$\sigma_{\mathrm{H}} = \frac{M_{\mathrm{RR}}(1) - D_1^2 - D_2\sigma_{\mathrm{R}} - D_3}{B_1 D_4}, \tag{30}$$
$$\sigma_{\mathrm{E}} = \frac{M_{\mathrm{RR}}(1) - D_2\sigma_{\mathrm{R}} - D_3 - B_1 D_4\sigma_{\mathrm{H}}}{A_1 D_1}, \tag{31}$$

where, $A_1 = \frac{\Gamma(2)}{\sqrt{2}\Gamma(1.5)}$ and $B_1 = \frac{\Gamma(1)}{\sqrt{\pi}\Gamma(1.5)}$.

In this instance, the first four orders are obtained through a combination of special bandwidth parameters, μ_n, and bandwidth parameters, α_n:

$$M_{\mathrm{RR}}(1) \approx \rho\mu_1^{-0.96}, \qquad M_{\mathrm{RR}}(2) \approx \rho\mu_1^{-0.02},$$
$$M_{\mathrm{RR}}(3) \approx \rho\mu_{0.52}, \qquad M_{\mathrm{RR}}(4) \approx \rho\mu_{0.55}, \tag{32}$$

where, $\rho = \alpha_1^{1.1}\alpha_2^{0.9}$ and $\mu_n = \frac{\lambda_{(n+0.01)}}{\sqrt{\lambda_{0.01}\lambda_{(2n+0.01)}}}$.

2.2.11. Wu method

Wu et al. (2023) developed an empirical formula for broadband random loadings based on Monte Carlo simulations of standard spectra. The fatigue damage is calculated as:

$$d_{\mathrm{WU}} = \nu_{\mathrm{p}}\lambda_0^{k/2} C^{-1} M_k, \tag{33}$$

where M_k is the rainflow stress range distribution moment, defined as:

$$M_k = \sum_{i=0}^{3}\sum_{j=0}^{i} a_{ij}\epsilon_1^{i-j}\epsilon_2^j. \tag{34}$$

The relationship between M_k and the spectral bandwidth parameters ϵ_1 and ϵ_2 was defined through a three-degree polynomial fitting by least squares fitting method, where a_{ij} denotes the fitting coefficient (Wu et al., 2023).

2.2.12. Jiao–Moan method

Jiao and Moan (1990) introduced a spectral approach to assess fatigue damage caused by bimodal processes, incorporating low-frequency (LF) and high-frequency (HF) components, which are assumed to be associated with current and wave effects, respectively. Their research revealed that bimodal processes in TD exhibit distinct small- and large-amplitude cycles. Consequently, the overall fatigue damage is the sum of damages from these respective components (Zorman et al., 2023):

$$D_{\mathrm{Y}} = D_{\mathrm{H}} + D_{\mathrm{P}}, \tag{35}$$

where D_{H} represents the fatigue damage due to the small-amplitude process (which is directly related to the HF component), and D_{P} is the damage due to the large-amplitude process $R_{\mathrm{P}}(t) = R_{\mathrm{H}}(t) + R_{\mathrm{L}}(t)$ (which is the HF envelope process plus the LF envelope process).

D_{H} is computed following Eq. (5) from the narrow-band approximation method, focusing solely on the HF response. In contrast, D_{P} is obtained by inserting the PDF, $p_{R_{\mathrm{P}}}(s)$, and mean zero up-crossing rate, $\nu_{0,\mathrm{P}}$, of the large-amplitude process in Eq. (4).

Since both the LF and HF components are considered narrow-banded and Gaussian, their PDFs are Rayleigh processes. Thus, the PDF of $R_{\mathrm{P}}(t)$ is obtained from the convolution of two Rayleigh distributions:

$$p_{R_{\mathrm{P}}}(s) = \lambda_1^* s e^{-\frac{s^2}{2\lambda_1^*}} + \lambda_2^* s e^{-\frac{s^2}{2\lambda_2^*}} + \sqrt{2\pi\lambda_1^*\lambda_2^*}(s^2-1)e^{-\frac{s^2}{2}}\left[\Phi\left(\sqrt{\frac{\lambda_1^*}{\lambda_2^*}}s\right) + \Phi\left(\sqrt{\frac{\lambda_2^*}{\lambda_1^*}}s\right) - 1\right], \tag{36}$$

where $\Phi(\cdot)$ represents the standard normal distribution function.

This method only accounts for the contribution of $P(t)$ when the LF component is significant (λ_1^* is large — although no limits are established for what is considered large). In that case, $p_{R_{\mathrm{P}}}(s)$ is approximated as:

$$p_{R_{\mathrm{P}}}(s) \approx \lambda_1^* s e^{-\frac{s^2}{2\lambda_1^*}} + \sqrt{2\pi\lambda_1^*\lambda_2^*}(s^2-1)e^{-\frac{s^2}{2}}\Phi\left(\sqrt{\frac{\lambda_2^*}{\lambda_1^*}}s\right). \tag{37}$$

The mean zero up-crossing rate of the large-amplitude process, $\nu_{0,\mathrm{P}}$, is obtained with the following equation:

$$\nu_{0,\mathrm{P}} = \lambda_1^* \nu_{0,1} \sqrt{1 + \frac{\lambda_2^*}{\lambda_1^*} \left(\frac{\nu_{0,2}}{\nu_{0,1}} \delta_2 \right)^2}, \tag{38}$$

where subscripts 1 and 2 correspond to the LF and HF components, respectively, λ_i^* represents the normalised variance of the component, and δ_2 is Vanmarcke (1972)'s bandwidth parameter.

To conclude, Jiao and Moan integrated the damage assessment formulations for both small- and large-amplitude cycles into a single closed-form correction factor, ρ_{JM}, that is multiplied to the narrow-band damage of the whole process obtained with Eq. (5):

$$\rho_{\mathrm{JM}} = \frac{\nu_{0,\mathrm{P}}}{\nu_{0,\mathrm{Y}}} \left[{\lambda_1^*}^{\frac{k}{2}+2} \left(1 - \sqrt{\frac{\lambda_2^*}{\lambda_1^*}} \right) + \sqrt{\pi \lambda_1^* \lambda_2^*} \frac{k \Gamma\left(\frac{k}{2} + \frac{1}{2}\right)}{\Gamma\left(\frac{k}{2} + 1\right)} \right] + \frac{\nu_{0,2}}{\nu_{0,\mathrm{Y}}} {\lambda_2^*}^{\frac{k}{2}}, \tag{39}$$

where $\nu_{0,\mathrm{Y}}$ is the mean zero up-crossing rate of the whole process.

2.2.13. Dual narrow-band method

The dual narrow-band approach is highly recommended by offshore standards such as DNV (2021) and API (2005). This method, which is rooted in the Jiao–Moan approach, involves the calculation of damage using Eq. (39). In these standards, Vanmarcke's bandwidth parameter δ_2 is fixed to 0.1.

2.2.14. Gao–Moan method

Based on the JM method (see Section 2.2.12), Gao and Moan (2008) proposed an extended version for trimodal cases by considering an ideal trimodal signal, in which the stress process consists of the sum of three narrow-band random components with well-separated central frequencies:

$$Y(t) = X_{\mathrm{HF}}(t) + X_{\mathrm{MF}}(t) + X_{\mathrm{LF}}(t), \tag{40}$$

where subscripts HF, MF, and LF refer to the high, intermediate, and low frequency components, respectively.

Following the same principle as Jiao and Moan (1990), fatigue damage is estimated as the sum of three equivalent amplitude processes that take into account the interactions between the three frequency components:

$$D_{\mathrm{Y}} = D_{\mathrm{H}} + D_{\mathrm{P}} + D_{\mathrm{Q}}, \tag{41}$$

where D_{H} represents the fatigue damage due to the small-amplitude process (which is directly related to the HF component), D_{P} is the damage due to the middle-amplitude process $R_P(t) = R_{\mathrm{H}}(t) + R_{\mathrm{M}}(t)$ (which is the HF envelope process plus the MF envelope process), and D_{Q} is the damage due to the large-amplitude process $R_Q(t) = R_{\mathrm{H}}(t) + R_{\mathrm{M}}(t) + R_{\mathrm{L}}(t)$ (which is the HF envelope process plus the MF envelope process and the LF envelope process).

Each individual damage assessment is obtained by inserting the PDF of the amplitude process in Eq. (4). Since the LF, MF, and HF components are considered narrow-banded and Gaussian, their PDFs are all Rayleigh processes, and both $R_P(t)$ and $R_Q(t)$ are Rayleigh sum processes with two and three components, respectively.

However, the Gao and Moan method has been excluded from the analysis as it is specifically designed for trimodal processes, whereas the present study focuses on bimodal signals.

2.2.15. Sakai–Okamura method

Sakai and Okamura (1995) proposed that in the case of bimodal loads, the total damage can be simply represented as the summation of two narrow-band damages, one associated with the LF component and the other with the HF component, each obtained following Eq. (5) (Zorman et al., 2023). Consequently, this method does not account for the interactions between LF and HF components. The closed-form solution is presented as follows:

$$d_{\mathrm{SO}} = \frac{2^{k/2}}{2\pi C} \Gamma\left(1 + \frac{k}{2}\right) \left[\lambda_{0,\mathrm{LF}}^{(k-1)/2} \lambda_{2,\mathrm{LF}}^{1/2} + \lambda_{0,\mathrm{HF}}^{(k-1)/2} \lambda_{2,\mathrm{HF}}^{1/2} \right]. \tag{42}$$

2.2.16. Fu–Cebon method

The methodology presented by Fu and Cebon (2000) implies that, for bimodal spectra, two amplitude cycles can be distinguished; a large-amplitude cycle with a low frequency rate ($\nu_{0,\mathrm{l}}^+ = \nu_{0,\mathrm{LF}}^+$) and an amplitude composed by the combination of the LF and HF components, and a small-amplitude cycle with an amplitude which approximately coincides with the HF component and a rate calculated by subtracting the LF rate from the HF rate ($\nu_{0,\mathrm{s}}^+ = \nu_{0,\mathrm{HF}}^+ - \nu_{0,\mathrm{LF}}^+$).

Since both LF and HF components of the bimodal signal are assumed to be narrow-banded, they are modelled using Rayleigh distributions. Small cycles, approximated using the HF component amplitude, are evaluated using Eq. (5) from the narrow-band approximation method.

Large-amplitude cycles, however, involve a convolution process, combining LF and HF distributions, to obtain their PDF, $p_{\mathrm{a_l}}(S)$:

$$p_{\mathrm{a_l}}(s) = p_{\mathrm{HF+LF}}(s) = \frac{1}{\lambda_{0,\mathrm{LF}} \lambda_{0,\mathrm{HF}}} e^{-\frac{s^2}{2\lambda_{0,\mathrm{HF}}^2}} \int_0^s (sy - y^2) e^{-Uy^2 + Vsy} \, \mathrm{d}y, \tag{43}$$

where $U = \frac{1}{2\lambda_{0,\mathrm{LF}}} + \frac{1}{2\lambda_{0,\mathrm{HF}}}$ and $V = \frac{1}{\lambda_{0,\mathrm{HF}}}$.

This combined PDF, $p_{\mathrm{a_l}}(s)$, is then integrated into Eq. (4) to compute the damage caused by large cycles.

According to Fu and Cebon (2000), Eq. (43) has no analytical solution. However, driven by difficulties in achieving numerical solutions, Benasciutti and Tovo (2007) observed that the definition of large cycles coincides with the one provided by the JM method. Consequently, the distribution described in Eq. (43) must be equivalent to Eq. (36). Following this insight, Low enhanced the large cycle damage formula by employing a binomial series expansion, leading to the derivation of an analytical solution (Low, 2010):

$$d_{\mathrm{l,\ FC}} = \frac{2^{3/2} \nu_{0,\mathrm{LF}}^+}{C} \sum_{j=0}^{k} \binom{k}{j} \sigma_{\mathrm{HF}}^j \sigma_{\mathrm{LF}}^{k-j} \Gamma\left(1 + \frac{j}{2}\right) \Gamma\left(1 + \frac{k-j}{2}\right), \tag{44}$$

where σ_{HF} and σ_{LF} are the standard deviations of the HF and LF components, respectively.

2.2.17. Modified Fu–Cebon method

Benasciutti and Tovo (2007) further improved the Fu–Cebon method (see Section 2.2.16) by making some small yet relevant changes. While both JM (see Section 2.2.12) and FC methods integrate LF and HF components in the large cycle amplitudes, JM associates the large-amplitude cycles to the envelope process $P(t)$. Hence, the large cycle rate, $\nu_{0,\mathrm{l}}^+$, is approximated by the mean zero up-crossing frequency of $P(t)$, $\nu_{0,\mathrm{P}}$ (Benasciutti, 2012).

This approximation was deemed more accurate by Benasciutti and Tovo as it makes $\nu_{0,\mathrm{l}}^+$ dependent on the relative contributions of both LF and HF components, as opposed to the FC case, where it only depends on the LF process.

For small cycles, Benasciutti and Tovo coincide with FC in that not all cycles associated with the HF process exhibit small amplitudes, and thus those large cycles must be subtracted from the total count of small cycles. Following the previous line of reasoning, the subtracted term should be updated to $\nu_{0,\mathrm{P}}$, leaving $\nu_{0,\mathrm{s}}^+ = \nu_{0,\mathrm{HF}}^+ - \nu_{0,\mathrm{P}}$.

Therefore, the total damage assessed by this modified Fu–Cebon method (MFC) is computed following Section 2.2.16 and replacing $\nu_{0,\mathrm{LF}}^+$ by $\nu_{0,\mathrm{P}}$.

2.2.18. Low's bimodal method

Low (2010) devised a method tailored for bimodal processes by thoroughly examining a representative bimodal signal combined with RFC. This approach highlighted two significant effects concerning the assessment of damage for both large- and small-amplitude cycles. Firstly, unlike earlier techniques that directly correlated the amplitude of small cycles with that of the HF component, it was discovered that the presence of an LF component caused a modification in the amplitude of small cycles.

Therefore, in the case of small-amplitude cycles, the damage is calculated by integrating across the probability domains of the HF and LF components, as well as the phase angle Θ, weighted by their joint PDF. As all three terms are independent, in this case, the joint PDF can be decomposed into the product of the individual PDFs:

$$d_{s_{\mathrm{LWB}}} = \frac{\nu^{+}_{0,\mathrm{HF}} - \nu^{+}_{0,\mathrm{LF}}}{C} \int_0^{\infty} \int_{\frac{\pi}{4B}}^{\frac{\pi}{2}} \int_{\varepsilon(s_{\mathrm{LF}},\theta)}^{\infty} [s_{\mathrm{LF}} - \varepsilon(s_{\mathrm{LF}},\theta)]^k \, p_{\mathrm{a,HF}}(s_{\mathrm{HF}}) p_{\Theta}(\theta) p_{\mathrm{a,LF}}(s_{\mathrm{LF}}) \, \mathrm{d}s_{\mathrm{HF}} \, \mathrm{d}\theta \, \mathrm{d}s_{\mathrm{LF}}, \tag{45}$$

where $p_{\mathrm{a,HF}}$, and $p_{\mathrm{a,LF}}$ denote the Rayleigh PDFs of the HF and LF amplitude components, respectively; $p_{\Theta}(\theta)$ denotes the uniform PDF of the phase angle from $\frac{\pi}{4\beta}$ to $\frac{\pi}{2}$; and $\varepsilon(s_{\mathrm{LF}},\theta)$, obtained following Eq. (46), is the discrepancy between the HF and small cycle stress amplitudes.

$$\varepsilon(s_{\mathrm{LF}},\theta) = \frac{\pi}{2B} s_{\mathrm{LF}} \sin\theta, \tag{46}$$

where B describes the spacing between LF and HF components:

$$B = \frac{\nu^{+}_{0,\mathrm{HF}}}{\nu^{+}_{0,\mathrm{LF}}}. \tag{47}$$

Regarding large-amplitude cycle damage, previous methods (Fu and Cebon, 2000; Jiao and Moan, 1990) associate the large cycle amplitude directly with the sum of the LF component and the envelope of the HF component. Nevertheless, Low (2010) discovered that HF and LF components seldom coincide and are frequently offset by a phase Ψ. In such instances, the large-amplitude cycles are smaller than the direct sum of LF and HF processes.

The damage is once again estimated by a triple integral over the probability domains of the HF and LF components, and Ψ:

$$d_{\mathrm{l_{LWB}}} = \frac{\nu^{+}_{0,\mathrm{LF}}}{C} \int_0^{\infty} \int_0^{\infty} \int_0^{\pi} [S_{\mathrm{l}}(s_{\mathrm{LF}}, s_{\mathrm{HF}}, \psi)]^k \, p_{\Psi}(\psi) p_{\mathrm{a,HF}}(s_{\mathrm{HF}}) p_{\mathrm{a,LF}}(s_{\mathrm{LF}}) \, \mathrm{d}\phi \, \mathrm{d}s_{\mathrm{HF}} \, \mathrm{d}s_{\mathrm{LF}}, \tag{48}$$

where $p_{\Psi}(\psi)$ denotes the uniform PDF of the phase from 0 to π, and $S_l(s_{\mathrm{LF}}, s_{\mathrm{HF}}, \psi)$ is the large stress amplitude function:

$$S_{\mathrm{l}}(s_{\mathrm{LF}}, s_{\mathrm{HF}}, \psi) = s_{\mathrm{LF}} \cos(c(s_{\mathrm{LF}}, s_{\mathrm{HF}})\psi) + s_{\mathrm{HF}} \cos(Bc(s_{\mathrm{LF}}, s_{\mathrm{HF}}) - 1)\psi, \tag{49}$$

where

$$c(s_{\mathrm{LF}}, s_{\mathrm{HF}}) = \frac{s_{\mathrm{HF}} B}{s_{\mathrm{LF}} + s_{\mathrm{HF}} B^2}. \tag{50}$$

The total damage is calculated by combining the damage from small and large amplitude cycles. To enhance computational efficiency, Low introduced an analytical expression for the innermost integral using a series expansion technique, reducing the integration to two dimensions (Low, 2010; Zorman et al., 2023).

2.2.19. Low method

Low (2014) introduced another method for damage assessment in bimodal processes with a focus on accurate prediction through a simple and user-friendly formula. The methodology included building a thorough database from numerical simulations and RFC outcomes to then fit the data into a surrogate model that corresponds with a correction factor to the narrow-band damage estimated following Eq. (5):

$$d_{\mathrm{LOW}} = \frac{L(\sigma^2_{\mathrm{HF}}, B, k)}{\sqrt{1 - \sigma^2_{\mathrm{HF}} + B^2 \sigma^2_{\mathrm{HF}}}} d_{\mathrm{NB}}, \tag{51}$$

where σ^2_{HF} is the normalised variance of the HF process, B is the ratio of frequencies obtained as shown in Eq. (47) and $L(\sigma^2_{\mathrm{HF}}, B, k)$ is the LF damage ratio:

$$L = \left[b_1 \sigma_{\mathrm{HF}} + b_2 \sigma^2_{\mathrm{HF}} - (b_1 + b_2)\sigma^3_{\mathrm{HF}} + \sigma^k_{\mathrm{HF}} \right](B - 1) + 1,$$

$$b_1 = (1.111 + 0.7421k - 0.0724k^2)B^{-1} + (2.403 - 2.483k)B^{-2}, \tag{52}$$

$$b_2 = (-10.45 + 2.65k)B^{-1} + (2.607 + 2.63k - 0.0133k^2)B^{-2}.$$

This approximation holds true for $3 \leq B < \infty$, $0 \leq \sigma^2_{\mathrm{HF}} \leq 1$, and $3 \leq k \leq 8$ (Low, 2014).

2.2.20. Han–Ma method

Han et al. (2016) developed a spectral method that accounts for the combination of LF and HF components. When the two components are independent narrow-band Gaussian processes, the combined response is assumed to be the sum of two sine waves. Following this premise, Han et al. (2016) derived a simple formula that combines the damages of the LF and HF components:

$$d_{\mathrm{HMa}} = \left(d^{2/k}_{\mathrm{NB,LF}} + d^{2/k}_{\mathrm{NB,HF}} \right)^{k/2}, \tag{53}$$

where $d_{\mathrm{NB,LF}}$ and $d_{\mathrm{NB,HF}}$ are obtained using Eq. (5) for the LF and HF components, respectively.

2.2.21. Single moment method

Lutes and Larsen (1990) developed an empirical formula:

$$d_{\mathrm{SM}} = \frac{2^{\frac{k}{2}}}{2\pi C} \Gamma\left(1 + \frac{k}{2}\right) \left(\lambda_{\frac{2}{k}}\right)^{\frac{k}{2}}, \tag{54}$$

that depends on the spectral moment $\lambda_{2/k}$. Based on the patterns observed in the results derived from extensive simulations and rainflow analysis, this method has been proven to provide accurate results when working with bimodal spectra (Benasciutti, 2012; Larsen and Lutes, 1991; Lutes and Larsen, 1990).

2.2.22. Lotsberg method

The Lotsberg (2005) method is a spectral damage assessment technique tailored for bimodal stress processes. It utilises the narrow-band approximation method 2.2.1 to assess LF and HF damages separately. Moreover, the method combines these distinct damage evaluations through a nonlinear combination to determine the total damage:

$$d_{\mathrm{LB}} = d_{\mathrm{NB,HF}} \left(1 - \frac{\nu^{+}_{0,\mathrm{LF}}}{\nu^{+}_{0,\mathrm{HF}}} \right) + \nu^{+}_{0,\mathrm{LF}} \left(a^{\frac{1}{k}} + b^{\frac{1}{k}} \right), \tag{55}$$

where,

$$a = \frac{d_{\mathrm{NB,HF}}}{\nu^{+}_{0,\mathrm{HF}}}, \tag{56}$$

$$b = \frac{d_{\mathrm{NB,LF}}}{\nu^{+}_{0,\mathrm{LF}}}, \tag{57}$$

and $d_{\mathrm{NB,HF}}$, and $d_{\mathrm{NB,LF}}$ are obtained using Eq. (5) for the HF and LF components, respectively.

This method has lately become popular in DNV specifications for offshore steel structures (Zorman et al., 2023).

2.2.23. Huang–Moan method

Inspired by the practicality of Lotsberg's formula (see Section 2.2.22), Huang and Moan (2006) devised a method that estimates fatigue damage as a nonlinear combination of the LF and HF damage contributions. They recognised that, while Lotsberg's method was convenient for practical applications, it tended to overestimate damage by a factor of up to two based on their results. Consequently, to address this issue and improve accuracy, Huang and Moan developed another explicit formula:

$$d_{\mathrm{HM}} = \frac{\left[a^{\frac{2}{k}} + b^{\frac{2}{k}}\right]^{\frac{k-2}{2}} \left[(\nu^{+}_{0,\ \mathrm{HF}})^2 a^{\frac{2}{k}} + (\nu^{+}_{0,\ \mathrm{LF}})^2 b^{\frac{2}{k}}\right]^{\frac{3}{2}}}{\left[(\nu^{+}_{0,\ \mathrm{HF}})^4 a^{\frac{2}{k}} + (\nu^{+}_{0,\ \mathrm{LF}})^4 b^{\frac{2}{k}}\right]^{\frac{1}{2}}}, \tag{58}$$

where a and b are obtained using Eqs. (56) and (57), respectively.

2.2.24. Bands method

The Bands method was proposed by Braccesi et al. (2015) on the basis that if a PSD function of a stress signal can be divided into a set of sufficiently narrow bands, each of the bands could be associated with a Rayleigh distribution.

To enable the combination of damage from each band, it is necessary for these bands to have the same frequency. To achieve this condition, the bands, represented by their respective central frequencies ($\nu^{+}_{0,i}$), are adjusted to a reference central frequency ($\nu^{+}_{0,\mathrm{ref}}$):

$$\lambda_{0,i,\mathrm{ref}} = \lambda_{0,i}\left(\frac{\nu^{+}_{0,\mathrm{ref}}}{\nu^{+}_{0,i}}\right)^{-2/k}, \tag{59}$$

where $\lambda_{0,\ i,\ \mathrm{ref}}$ is the zero-order moment of band i "moved" to the reference frequency.

Then, the zero-order moment of the whole process can be calculated as:

$$\lambda_{0,\mathrm{ref}} = \sum_{i=1}^{m} \lambda_{0,i,\mathrm{ref}}. \tag{60}$$

The total damage is estimated using Eq. (5) from the narrow-band approximation method, with the variance and number of cycles equal to $\lambda_{0,\mathrm{ref}}$ and $\nu^{+}_{0,\mathrm{ref}}$, respectively:

$$d_{\mathrm{BM}} = \nu^{+}_{0,\mathrm{ref}} C^{-1}\left(\sqrt{2\lambda_{0,\mathrm{ref}}}\right)^{k} \Gamma\left(1+\frac{k}{2}\right). \tag{61}$$

This method is particularly favourable in terms of computational efficiency and simplicity (Braccesi et al., 2015).

2.2.25. Gao–Zheng method

Gao and Zheng (2019) introduced a spectral method for bimodal processes that accounts for the interactions between LF and HF components. The proposed method is based on the findings of Benasciutti et al. (2013), where it was suggested that the damage of broadband processes can be estimated through a spectral decomposition technique. Therefore, the spectra of the bimodal processes are separated into N infinitesimal frequency bands:

$$\lambda^{\mathrm{LF}}_{2/k} = \sum_{i=1}^{N} \left(\omega^{\mathrm{LF}}_{i}\right)^{2/k} W_x\left(\omega^{\mathrm{LF}}_{i}\right) \Delta\omega^{\mathrm{LF}}, \tag{62}$$

$$\lambda^{\mathrm{HF}}_{2/k} = \sum_{i=1}^{N} \left(\omega^{\mathrm{HF}}_{i}\right)^{2/k} W_x\left(\omega^{\mathrm{HF}}_{i}\right) \Delta\omega^{\mathrm{HF}}, \tag{63}$$

$$\lambda^{\mathrm{LF\&HF}}_{2/k} = \sum_{i=1}^{N} \xi_i \sqrt{\left[\left(\omega^{\mathrm{LF}}_{i}\right)^{2/k} W_x\left(\omega^{\mathrm{LF}}_{i}\right) \Delta\omega^{\mathrm{LF}}\right]} \cdot \sqrt{\left[\left(\omega^{\mathrm{HF}}_{i}\right)^{2/k} W_x\left(\omega^{\mathrm{HF}}_{i}\right) \Delta\omega^{\mathrm{HF}}\right]}, \tag{64}$$

where ω_i is the central frequency of the ith frequency band, $\Delta\omega$ is the width of frequency bands, spectral moments $\lambda^{\mathrm{LF}}_{2/k}$ and $\lambda^{\mathrm{HF}}_{2/k}$ correspond to the LF and HF components, respectively, the cross term $\lambda^{\mathrm{LF\&HF}}_{2/k}$ reflects their interaction, and the term ξ_i is an empirically fitted coefficient that describes the degree of interaction between the LF and HF bands (Gao and Zheng, 2019).

The total fatigue damage is calculated as follows:

$$d_{\mathrm{GZ}} = \frac{2^{k/2}}{2\pi C}\Gamma\left(1+\frac{k}{2}\right)\left(\lambda^{\mathrm{LF}}_{2/k} + \lambda^{\mathrm{HF}}_{2/k} + \lambda^{\mathrm{LF\ HF}}_{2/k}\right)^{k/2}. \tag{65}$$

2.2.26. Improved bands method

Yuan et al. (2023) extended the Bands method proposed by Braccesi et al. (2015) (see Section 2.2.24) by considering the interactions between LF and HF components.

For well-separated bimodal spectra, the energy is focused around two separated frequencies, and, thus, according to Yuan et al. (2023), the error induced by translating both the LF and HF components to the same reference frequency cannot be ignored. Additionally, the combination rule adopted in the BM method does not consider the effect of the superimposed HF and LF components.

Consequently, following Eqs. (59) and (60), the summed zero-order moments $\lambda_{0,\mathrm{ref,HF}}$ and $\lambda_{0,\mathrm{ref,LF}}$ of the HF and LF processes, respectively, are determined relative to their corresponding reference frequencies, $\nu^{+}_{0,\mathrm{ref,HF}}$ and $\nu^{+}_{0,\mathrm{ref,LF}}$. Then, the HF process is shifted to the reference central frequency of the LF process, resulting in an equivalent zero-order spectral moment $\lambda_{0,\mathrm{ref,LF\&HF}}$. The cumulative zero-order spectral moment, $\lambda_{0,\mathrm{total}}$, for the bimodal process can be expressed as follows:

$$\lambda_{0,\mathrm{total}} = \lambda_{0,\mathrm{r,LF}} + \lambda_{0,\mathrm{r,LF\&HF}} = \lambda_{0,\mathrm{r,LF}} + \left(\frac{\nu^{+}_{0,\mathrm{ref,HF}}}{\nu^{+}_{0,\mathrm{ref,LF}}}\right)^{2/k} \lambda_{0\mathrm{r,HF}}\mu, \tag{66}$$

where the parameter μ is an empirical factor incorporated to address the combined effect of the HF and LF components (Yuan et al., 2023).

Finally, the total fatigue damage is estimated as:

$$d_{\mathrm{IBM}} = \nu^{+}_{0,\mathrm{ref,LF}} C^{-1}\left(\sqrt{2\lambda_{0,\mathrm{total}}}\right)^{k} \Gamma\left(1+\frac{k}{2}\right). \tag{67}$$

2.2.27. Petrucci–Zuccarello method

The method proposed by Petrucci and Zuccarello (2004) provides a damage estimation that accounts for the mean stress effect by incorporating the Goodman equivalent stress r_e, obtained following Eq. (68) (Goodman, 1919), in its formulation:

$$r_e = \frac{r}{1 - m/S_{\mathrm{u}}}, \tag{68}$$

where r is the stress range, m is the mean stress, and S_{u} is the tensile strength of the material.

Using the equivalent stress range, the general damage formulation in Eq. (4) is modified as follows:

$$d = \nu_{\mathrm{p}} C^{-1} \int_0^{+\infty} r_e^k p(r_e) dr_e = \nu_{\mathrm{p}} C^{-1} \chi_k, \tag{69}$$

where χ_k is the kth moment of the PDF, $p(r_e)$.

Petrucci and Zuccarello developed a simplified relationship that involves only two bandwidth parameters, α_1 and α_2, to obtain χ_k:

$$\chi_k = \lambda_0^{k/2} g(\alpha_1, \alpha_2, \gamma), \tag{70}$$

where γ is the ratio between the absolute maximum value of the stress process and S_{u}, $g(\cdot)$ is approximated as:

$$g(\alpha_1, \alpha_2, \gamma) = e^{\Psi(\alpha_1, \alpha_2, k, \gamma)}, \tag{71}$$

and $\Psi(\cdot)$ yields:

$$\Psi(\alpha_1, \alpha_2, k, \gamma) = \frac{\Psi_2 - \Psi_1}{6}(k-3) + \Psi_1 + \left[\frac{2}{9}(\Psi_4 - \Psi_3 - \Psi_2 + \Psi_1)(k-3) + \frac{4}{3}(\Psi_3 - \Psi_1)\right](\gamma - 0.15) \tag{72}$$

$$\begin{aligned}\Psi_1 &= -1.994 - 9.381\alpha_2 + 18.349\alpha_1 \\ &\quad + 15.261\alpha_2\alpha_1 - 1.483\alpha_2^2 - 15.402\alpha_1^2 \\ \Psi_2 &= 8.229 - 26.510\alpha_2 + 21.522\alpha_1 \\ &\quad + 27.748\alpha_2\alpha_1 + 4.338\alpha_2^2 - 20.026\alpha_1^2 \\ \Psi_3 &= -0.946 - 8.025\alpha_2 + 15.692\alpha_1 \\ &\quad + 11.867\alpha_2\alpha_1 + 0.382\alpha_2^2 - 13.198\alpha_1^2 \\ \Psi_4 &= 8.780 - 26.058\alpha_2 + 21.628\alpha_1 \\ &\quad + 26.487\alpha_2\alpha_1 + 5.379\alpha_2^2 - 19.967\alpha_1^2\end{aligned} \tag{73}$$

The RFC method, as described in Section 2.1, only considers the stress ranges, excluding the mean stress component. Similarly, the previously described spectral methods focus solely on stress range calculation. In contrast, the PZ method considers the mean stress effect, which results in higher damage values for tensile mean stresses. Consequently, this method has been omitted from the analysis, as the results would not be comparable.

Note that the codes used for the benchmarking study, including all the TD and spectral approaches described in this section, have been released in open-source and are available at https://github.com/MGEP-Fluidos/ORE-Structural-Integrity.git.

3. Benchmarking framework

To enable straightforward benchmarking of the methods, a scoring system similar to the approach outlined by Nesládek et al. (2022) is proposed in the present paper. This benchmarking framework categorises the methods based on their ease of implementation and the obtained results and contrasts them with their level of establishment. For each category, different features, considered relevant by the authors, have been taken into account.

Implementation Ease

- **Simple formulation:** This aspect evaluates the ease of replication based on the simplicity of the formulation. Methods can earn up to one point for explicitness: 1 point if it is a closed-form solution, 0.75 points if it is closed-form but within a loop, 0.5 points if integration is needed, 0.25 points if multiple integrals are involved, and 0 points if the provided formulation cannot consistently achieve a solution.
- **Parameter quantity:** Simplicity is further evaluated based on the number of parameters in the model, with fewer parameters indicating easier replication. Methods can earn a maximum of one point if only spectral moments are used. However, 0.25 points are subtracted for each additional parameter, such as bandwidth parameters or best-fitting parameters.
- **Convergence time:** Computational efficiency is evaluated based on convergence time, with methods converging faster receiving a maximum of one point. Simulations are performed with different signal lengths up to a maximum of 10,000 s (see Section 5.1). Points are assigned as follows: the maximum signal length is divided into five segments of 2000 s each. Methods converging within the first interval receive a score of one, and a deduction of 0.25 points is applied for every subsequent interval beyond which convergence is achieved.
- **Computational time:** Spectral methods are evaluated on a scale up to one point, determined by the computational time needed to perform the damage estimations. The computational times of each spectral method are normalised based on the time required by RFC. The scoring is derived from these normalised values. Table 2 illustrates the scores associated with the normalised time ranges.

Table 2
Score values applied for computational time.

Normalised computational time	Score
[0 – 0.2]	1
(0.2 – 0.4]	0.75
(0.4 – 0.6]	0.5
(0.6 – 0.8]	0.25
(0.8 – 1]	0

Table 3
Scoring system applied for precision and accuracy.

Criterion [%]	Score
[0 – 5]	2
(5 – 10]	1.5
(10 – 15]	1
(15 – 30]	0.5
> 30	0

Note: IQR scores are multiplied by 0.75, outliers by 0.25.

Result Suitability

- **Risk:** Methods yielding non-conservative results are penalised, meaning that the damage is underestimated compared to the reference RFC technique. A deduction of 0.5 points is applied if both the mean and tail of the results distribution are non-conservative, and 0.25 points if only one is non-conservative.
- **Precision:** Precision assesses results' repeatability, indicating how consistent outcomes are. This aspect is evaluated based on the interquartile range (IQR) and the outliers of the relative damage difference results obtained for the analysed cases via Eq. (74). Methods receive up to two points based on their precision. Specifically, out of the two points, 1.5 are assigned based on the IQR, while the remaining 0.5 is assigned based on the outliers. Outliers represent maximum errors but are points that fall outside the overall trend of the data. Thus, while it is important to consider them, a greater weight is assigned to the overall trend of the results. Table 3 shows the criteria followed.
- **Accuracy:** Accuracy evaluates how closely mean relative damage difference values align with the RFC damage. Methods are scored based on the accuracy of their mean values, with a maximum of two points. Table 3 shows the criteria followed.

The above-mentioned features are considered to evaluate each method's performance, with a maximum achievable score of eight points. An additional point is provided based on a non-technical aspect.

Level of Establishment

- **Cite rate:** This feature measures each method's acceptance and popularity through their citations per year. Methods with higher citation rates, indicating greater acceptance, are awarded up to one point. To determine the scores, the citations of all methods are summed, and each method's citations are then normalised based on the total value. These normalised percentages are divided into five percentiles, and these percentile values serve as thresholds for the scores.
- **Recommendation in offshore standards:** Methods recommended in offshore standards receive an automatic score of one, reflecting their recognised status within established industry guidelines.

The cumulative score, totalling eight plus one points, provides a comprehensive perspective on the suitability of these methods for assessing fatigue loads in offshore mooring systems. It is important to note that the definition of these scores entails a degree of subjectivity.

4. Case study

For the sake of clarity, this study is exclusively focused on WECs and mooring lines. Specifically on examining the catenary mooring system of the RM3 point absorber, a reference model developed by Sandia National Laboratories as part of the Reference Model Project (Neary et al., 2014). The WEC-based case study is assumed to be representative of other ORE systems, mooring configurations, and dynamic cables.

To enable a comparison of the selected spectral methods, the tension loadings analysed in this study are based on the specific characteristics and operational conditions of the RM3 device. Hence, this approach ensures a comprehensive evaluation in terms of the performance and accuracy of various methods for predicting fatigue damage for offshore applications.

4.1. WEC and mooring system characteristics

The design of the RM3 device incorporates a torus-like float that undergoes oscillatory motion in response to wave movements, operating in conjunction with a spar connected to a reaction plate that minimises its motion, thereby maximising the relative heave motion for optimal energy conversion (Fig. 6). This configuration enables the device to function as a two-body point absorber, efficiently converting wave energy into electrical power primarily through the heave oscillation of the float induced by incoming waves. The RM3 device employs a mooring system comprised of three mooring lines, each divided into two sections with a submerged buoy positioned between them, as illustrated in Fig. 6. The pertinent geometric data, as presented in Table 4, has been extracted from the details available in the open-source WEC-Sim code (NREL and Sandia, 2022).

In Section 2, various FIPs are mentioned for evaluating fatigue damage. However, in this study, the fatigue damage of the stud chains has been assessed using the S–N curve tailored to R3 grade steel, employing the Basquin expression (1910). The relevant properties, extracted from DNV (2021), are presented in Table 5.

Table 4
Summary of the main parameters that define the RM3 model and its mooring system setup (NREL and Sandia, 2022).

Floater mass	[kg]	7.2710^5
Floater inertia	[kg m^2]	
	Ixx	20907301
	Iyy	21306091
	Izz	37085481
Spar mass	[kg]	8.78310^5
Spar inertia	[kg m^2]	
	Ixx	94419615
	Iyy	94407091
	Izz	28542225
Chain Nominal Diameter	[mm]	144
Linear density	[kg/m]	126
Line stiffness (EA)	[N]	583.3810^6
S1 length	[m]	40
S2 length	[m]	240
Submerged buoy mass	[kg]	16 755

Table 5
S–N curve parameters employed in the study (DNV, 2021).

	C [MPa^k]	k
Stud chain	$1.2\ 10^{11}$	3

4.2. Loading conditions

Offshore structures experience complex and dynamic conditions influenced by elements like wind, waves, and currents. These factors lead to diverse loading conditions.

Mooring tensions caused by the hydrodynamic response of WECs consist of two primary frequency components: wave frequency (WF) and low frequency (LF). Fig. 7 illustrates these frequency components.

The wave frequency component characterises the mooring system's response to wave-induced dynamics. It accounts for the rapid tension oscillations that coincide with wave passage. These oscillations typically possess high frequencies and are of short duration, aligning with the characteristic wave periods.

In contrast, the low frequency component represents prolonged tension variations resulting from environmental factors like tidal forces, currents, and gradual environmental changes, as well as non-linear hydrodynamic effects such as nonlinear wave loading, wave-driven currents, or viscous effects. These variations occur over significantly longer time frames compared to the WF component.

As discussed in Section 1, assessing fatigue damage in offshore settings requires considering a broad range of sea states (SS). To expedite this process, synthetic tension signals inspired by hydrodynamic simulations have been generated instead of conducting individual numerical simulations for each case. The simulations were performed for 17 SS from the RM3 device site, located near Eureka in Humboldt County, California, as detailed in Neary et al. (2014). The wave direction was set to 0° for every sea state considered, and for the sake of simplicity, the analysed mooring line is the one coincident with this angle.

The utilisation of synthetic signals for rapid assessment is a common strategy in research, as demonstrated by other authors who have

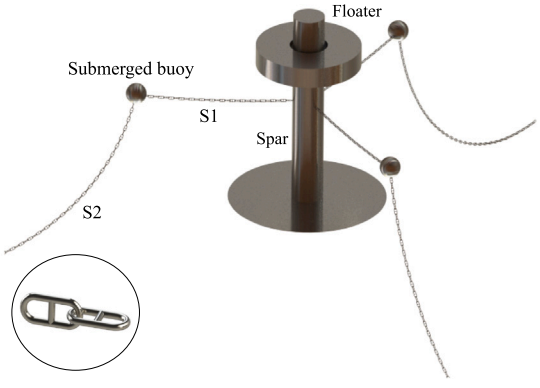

Fig. 6. RM3 mooring system representation.

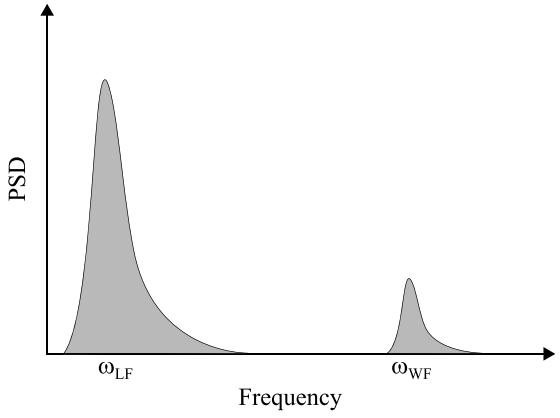

Fig. 7. Mooring line tension response power spectral density.

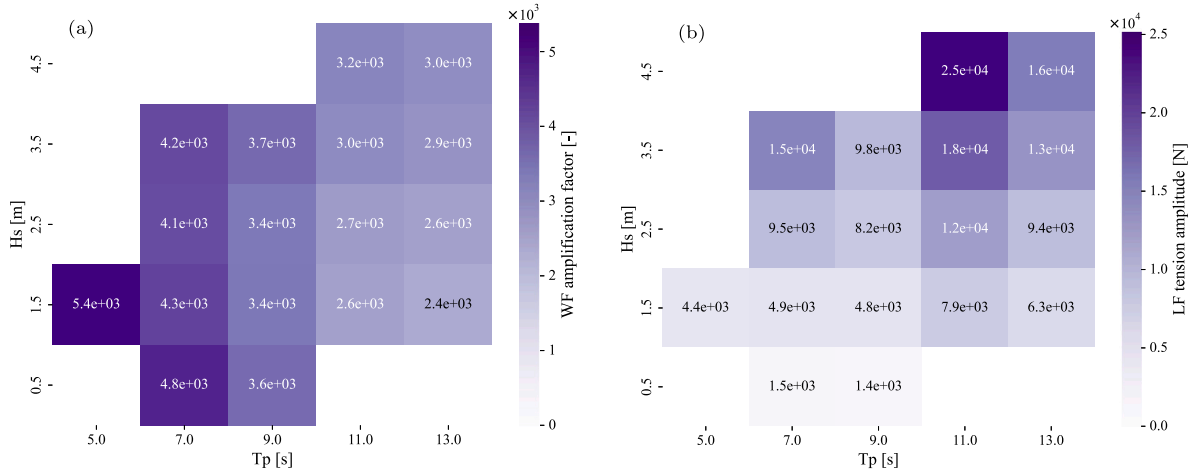

Fig. 8. Characteristic values of the mooring tension responses derived from the hydrodynamic simulations for the simulated SS: (a) WF tension component amplification factor, and (b) LF tension component amplitude.

employed similar methodologies (Llavori et al., 2020). By avoiding the resource-intensive numerical simulations for each SS, this approach enables a swift and cost-effective exploration of a wide range of conditions. The synthetic signals not only accelerate the assessment process but also enable a realistic representation of hydrodynamic complexities, achieving a balance between computational efficiency and characteristic modelling of environmental factors.

For this benchmarking analysis, the 17 simulated SS were extended to 70 generated via synthetic signal generation. Furthermore, to capture the variability within each SS, 50 realisations were generated for each using randomised seeds in the wave spectrum. The use of different seeds ensures a comprehensive analysis of the potential variability in the response. In total, 3500 synthetic signals (50 realisations for each of the 70 SS) were analysed, providing a robust data set for evaluating the performance of the assessed methodologies.

4.2.1. Wave frequency tension signals

To generate the WF components, the wave surface elevation is derived using the JONSWAP spectrum (Hasselmann et al., 1973), determined by the specified significant wave height (H_s) and peak period (T_p). In this study, 70 SS were created, covering a wide operational range for most common WEC locations, with H_s ranging from 0.1 m to 14 m and T_p from 4 s to 18 s.

Once the wave surface elevation is obtained, it is multiplied by an amplification factor to simulate the WF tension component. This amplification factor was determined by observing the mooring tension responses from the hydrodynamic simulations of the RM3 device performed via WEC-Sim, as detailed in Section 4.1.

Fig. 8(a) displays the observed amplification factors, with a maximum value of 5.4×10^3 and a minimum of 2.4×10^3. For simplicity and considering the small variation in values, the mean value from the observed results (3.5×10^3) was adopted. This choice is justified by the linearity of Miner's damage rule, ensuring that the benchmarking relationship remains unaffected.

4.2.2. Low frequency tension signals

The generation of the LF signals also relies on the JONSWAP spectrum. The significant amplitude and mean tensions for these components are derived from hydrodynamic simulations, as detailed in Section 4.1. Fig. 8(b) indicates that the amplitude exhibits a notable increase with growing H_s. Given that the simulations cover up to a H_s of 4.5 m, an extrapolation is applied to estimate amplitude values up to H_s of 14 m. Consequently, the amplitudes of LF synthetic signals range from 1×10^3 to 8×10^4 N. Concerning the mean tension, values remain constant across all SS, emphasising their high dependence on mooring characteristics. A mean tension value of 1.7×10^5 N is adopted.

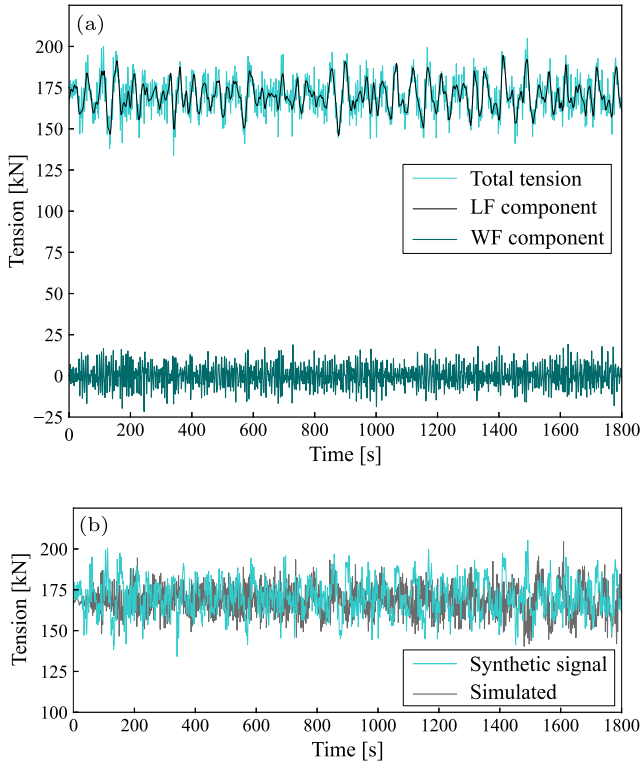

Fig. 9. Mooring line tension response: (a) synthetically generated response split up into LF and WF components, and (b) superimposed synthetic and simulated responses.

Fig. 9(a) shows a TD representation of one of the analysed SS, and Fig. 9(b) shows the superimposed synthetic and WEC-Sim simulated responses, demonstrating a good correlation between both signals.

5. Results and discussion

In this section, the damage assessment results of the spectral methods selected in Section 2.2 are presented, and their performance is assessed in terms of the reference (ground truth) damage, which is the damage estimated through the RFC method. In the literature, various indicators have been employed to assess the correctness of the results

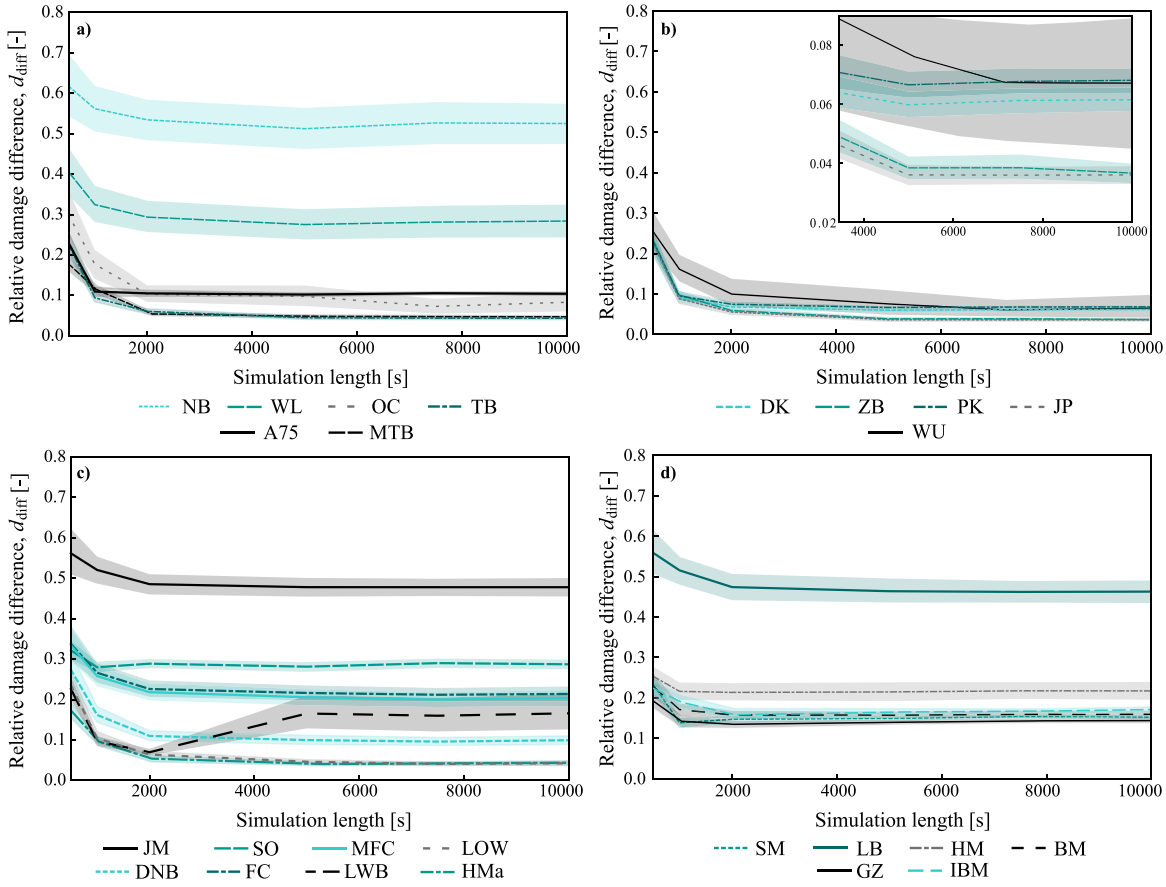

Fig. 10. Simulation length convergence patterns for each spectral method: (a) Narrow-band correction factor; (b) RFC approximation; (c) Cycle type damage combination; and (d) Narrow-band damage combination methods.

in terms of RFC damage. Some studies use either the relative damage difference (Braccesi et al., 2015; Xu and Soares, 2021; Zorman et al., 2023)

$$d_{\text{diff}} = \frac{|d_{\text{FD}} - d_{\text{RFC}}|}{d_{\text{RFC}}}, \tag{74}$$

or the normalised damage (Jun and Park, 2020; Park et al., 2014)

$$d_{\text{norm}} = \frac{d_{\text{FD}}}{d_{\text{RFC}}}, \tag{75}$$

where d_{FD} is the damage rate estimated with one of the spectral methods and d_{RFC} is the damage rate obtained with the RFC technique.

Eqs. (74) and (75) have been selected in this work to obtain insights into the accuracy, precision, and conservative or non-conservative nature of the spectral methods.

5.1. Convergence analysis

To ensure the reliability of the findings, a convergence analysis has been conducted with the aim of determining the appropriate signal length for comparing different methods. It should be noted that the results are affected by the length of the analysed tension signals. Thus, this analysis helps in selecting the optimal signal duration for a meaningful comparison among the various methods.

To capture the statistical parameters of wave conditions, SS are usually simulated over a three-hour time frame. Despite this, to minimise signal lengths without compromising result reliability, a convergence study has been performed. This study explores variations in damage using spectral methods across different simulation lengths, spanning from 100 s to nearly three hours (10,000 s).

In Fig. 10, the convergence patterns of the damage differences, along with a 95% confidence interval, are presented for each spectral method. Fig. 10 is divided into four graphs representing the four groups for broadband damage estimation, providing a clear overview of the convergence patterns. The A75, HM, and GZ methods are the first to converge at around 1000 s, followed by the TB, MTB, JM, DNB, SO, FC, MFC, SM, BM, and IBM methods at a simulation length of about 2000 s. The NB, OC, and WU methods are the last to converge at 7500 s, while the remaining methods converge around 5000 s. To ensure a fair and comparative analysis, all signals used in the study were generated for a consistent length of 7500 s.

5.2. Comparison of the damage estimations

The damage results for the simulated SS are presented in Fig. 11. For each SS, the mean value of the 50 realisations is considered. The graph shows fatigue damage computed via the TD model on the horizontal axis and fatigue damage provided by spectral methods on the vertical axis. The RFC damage serves as a reference, representing the target damage to be achieved by the spectral methods. Points below this line suggest non-conservative results, whereas points above indicate conservative outcomes, with the former being riskier for the design process, particularly in terms of fatigue. Similarly to Fig. 10, the graph has been divided into four parts, corresponding to the four groups of spectral methods selected for the benchmarking. Additionally, the points that fall outside the limits' bounds are depicted in the margin of the graph with an upward arrow, which indicates that the real position of these points is beyond the limits.

Fig. 11(a) provides a general view of damage results across all spectral methods. Due to the substantial data points, drawing definitive

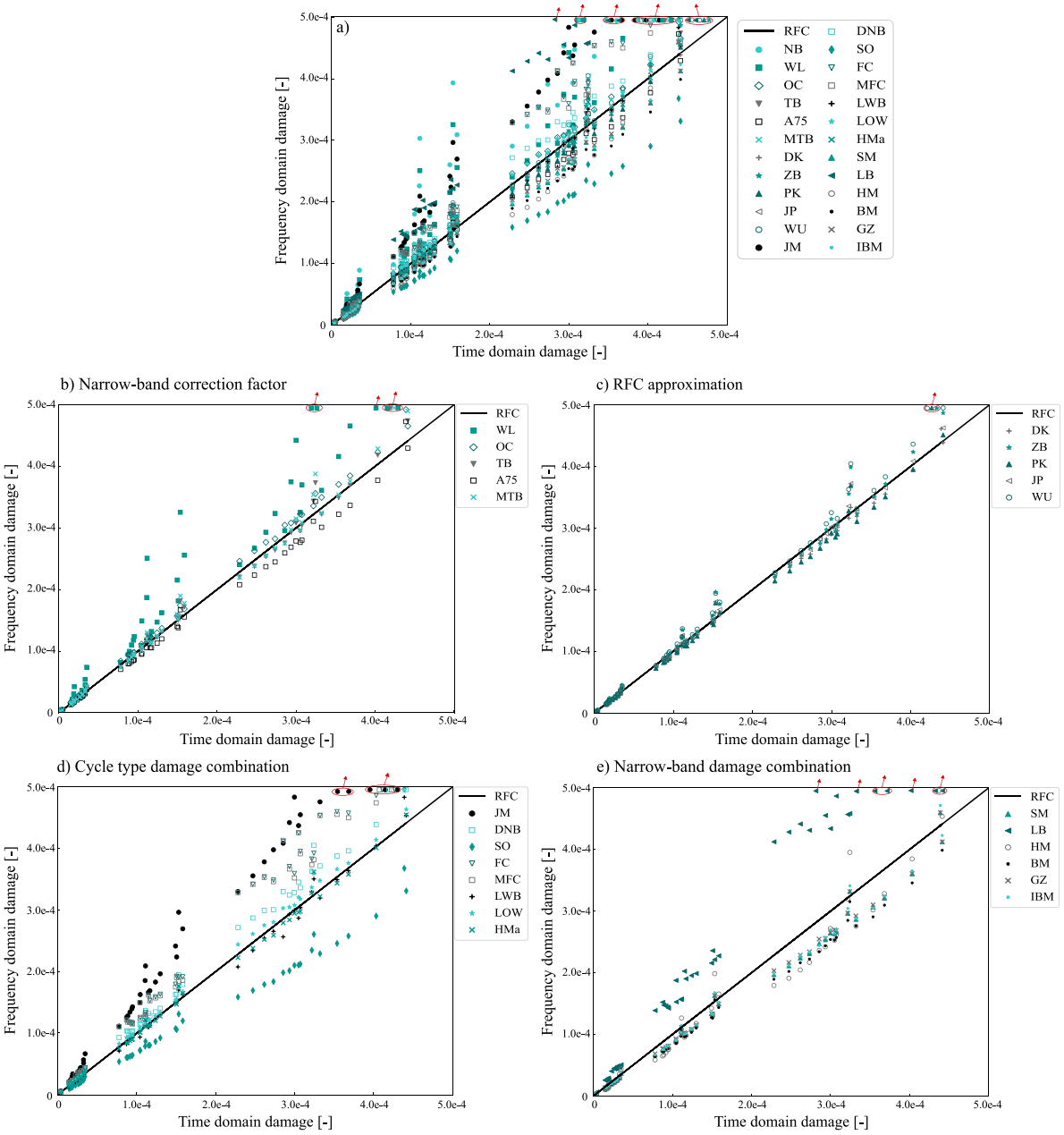

Fig. 11. Fatigue damage comparison of frequency and time domain methods: (a) All spectral models; (b) Narrow-band correction factor; (c) RFC PDF approximation; (d) Cycle type damage combination; and (e) Narrow-band damage combination models.

conclusions from this perspective is challenging. To enhance clarity, the graph has been segmented into four distinct groups based on the criteria identified in Section 2.2.

Narrow-band correction factor: In Fig. 11(b), attention is directed towards methods employing the narrow-band correction factor approach. Notably, the WL method consistently produces results that are highly overestimated. In a similar way, the OC method maintains a general trend toward conservatism; however, its results are more closely aligned with the reference line. Both TB, A75, and MTB exhibit a combination of over and underestimated results, fitted to the reference RFC damage. A variety of performances are showcased within this group.

RFC approximation: Fig. 11(c) depicts methods using the RFC PDF, or moment-based approximation. The five methods in this group demonstrate a spectrum of overestimations and underestimations that closely align with the RFC reference line. This group showcases a consistent pattern in performance.

Cycle type damage combination: In Fig. 11(d), an examination of methods based on the cycle type damage combination reveals distinct trends. The JM, FC, and MFC exhibit a tendency towards highly conservative estimations, with certain data points exceeding the graph's bounds. While also conservative, DNB and LOW deliver more suitable results. SO, LWB, and HMa, however, exhibit clearly non-conservative behaviour.

Narrow-band damage combination: Fig. 11(e) includes the results of methods utilising the narrow-band damage combination principle. Within this group, LB consistently yields conservative results, with highly overestimated damage values. Conversely, SM, HM, BM, GZ, and IBM lean towards non-conservative tendencies, generating mostly underestimated damage values.

To give insight into which methods provide overestimated results and which ones result in underestimations, all the damages have been normalised relative to the RFC damages following Eq. (75). Results are

Table 6
Damage mean relative difference and box-plot quartile values in percentage.

	Mean	Q1	Q3	IQR
NB	57	28	71	43
WL	32	9	42	33
OC	11	5	8	3
TB	4	2	5	2
A75	8	6	10	3
MTB	5	2	7	5
DK	4	3	5	2
ZB	5	2	5	3
PK	6	3	7	4
JP	3	1	3	2
WU	8	1	11	10
JM	50	43	57	13
DNB	15	10	18	8
SO	25	25	31	6
FC	26	20	33	13
MFC	25	17	33	16
LWB	3	1	5	4
LOW	6	4	7	3
HMa	4	2	5	3
SM	12	10	14	4
LB	52	43	65	22
HM	21	14	26	12
BM	15	14	18	4
GZ	11	10	13	3
IBM	12	10	14	4

plotted using boxplot diagrams, as shown in Fig. 12, where one is the target value (green line), showing that the FD value matches the RFC value.

Hence, the A75, DK, PK, SO, HMa, SM, HM, BM, GZ, and IBM methods provide mostly non-conservative results, while the NB, WL, OC, WU, JM, DNB, FC, MFC, LOW, and LB methods lead to conservative results. Regarding the TB, MTB, ZB, JP, and LWB methods, both conservative and non-conservative estimations can be observed, with their mean values closely aligning with the RFC reference.

From Fig. 12, it becomes apparent that the methods categorised within the RFC approximation group consistently yield results with minimal dispersion, closely following the RFC reference. Conversely, methods like NB and WL exhibit significant dispersion in their results, deviating notably from the RFC reference. While the OC method generally aligns well with the target, it is characterised by a notable presence of outliers, resulting in considerably overestimated damage values. Conversely, the HM method tends to underestimate damage values, enhanced due to the presence of outliers that skew the results towards lower damage values.

The relative damage differences have been estimated following Eq. (74) for each spectral method. Table 6 shows the main characteristics in terms of statistical metrics, such as the mean, quartiles, and IQR, which are used to evaluate the precision and accuracy aspects of each method in the designed scoring system. Among the methods, the NB model exhibits the largest mean damage difference (57%) and the greatest dispersion (43%). Following closely are the LB, JM, and WL methods, with mean damage differences of 52%, 50%, and 32% and IQR values of 22%, 13%, and 33%, respectively, far from the rest of the spectral methods. On the other hand, the methods that follow the RFC PDF approximation approach and TB, A75, MTB, LWB, LOW, and HMa exhibit the smallest combination of relative damage differences and IQR.

5.3. Comparison of the computational times

As outlined in Section 1, the primary advantage of spectral methods over RFC analysis lies in their computational efficiency. To quantify the potential time savings achievable through the adoption of spectral methods in fatigue assessment, computational times for each method in the benchmarking analysis have been recorded. Fig. 13 presents normalised computational times relative to RFC, where values below one indicate time reductions.

The results reveal that nearly all spectral methods, excluding LWB and IBM, yield substantial reductions in the time required for fatigue assessment. This aligns with the assertions found in the existing literature. Spectral methods such as NB, WL, OC, A75, DK, WU, JM, DNB, SO, LOW, HMa, SM, LB, HM, and GZ showcase time reductions exceeding 90%. Similarly, TB, MTB, PK, JP, FC, and MFC exhibit significant reductions ranging between 80% and 90%. Although less pronounced, ZB achieves a 56% reduction, and BM presents a 37% advantage over RFC. In the case of the BM method, the stress spectrum is segmented into small frequency bands, with damage computed for each band, likely contributing to its comparatively longer computational time.

In contrast, the LWB and IBM methods stand out as exceptions, demanding computational times that exceed those of the RFC method. The IBM follows a similar principle to the BM. However, it divides the frequency bands into LF and HF components, effectively repeating the same procedure twice. This repetition could be the cause of its longer

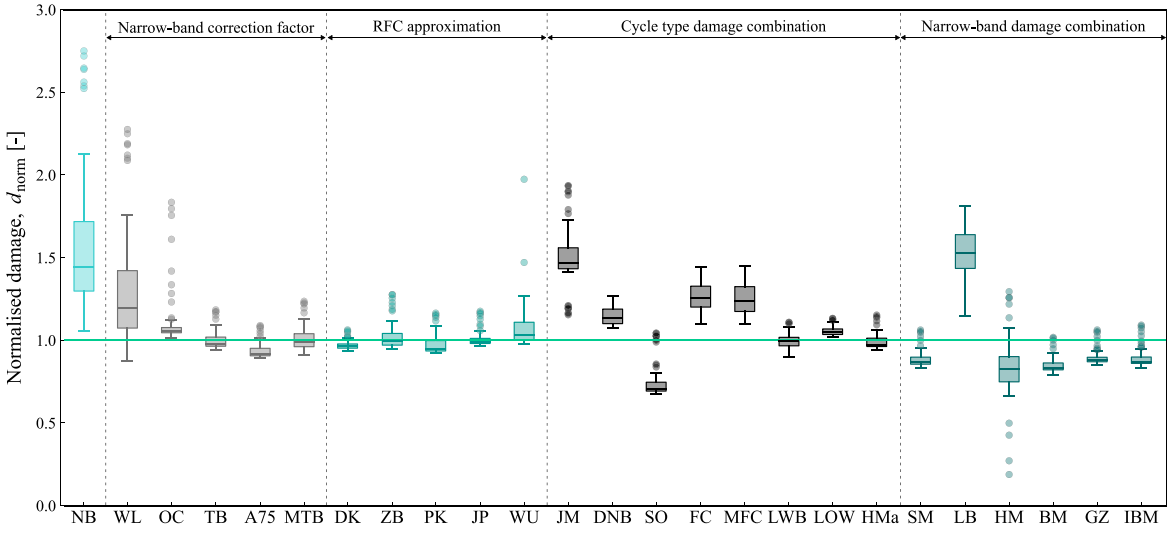

Fig. 12. Normalised damage comparison for each spectral method.

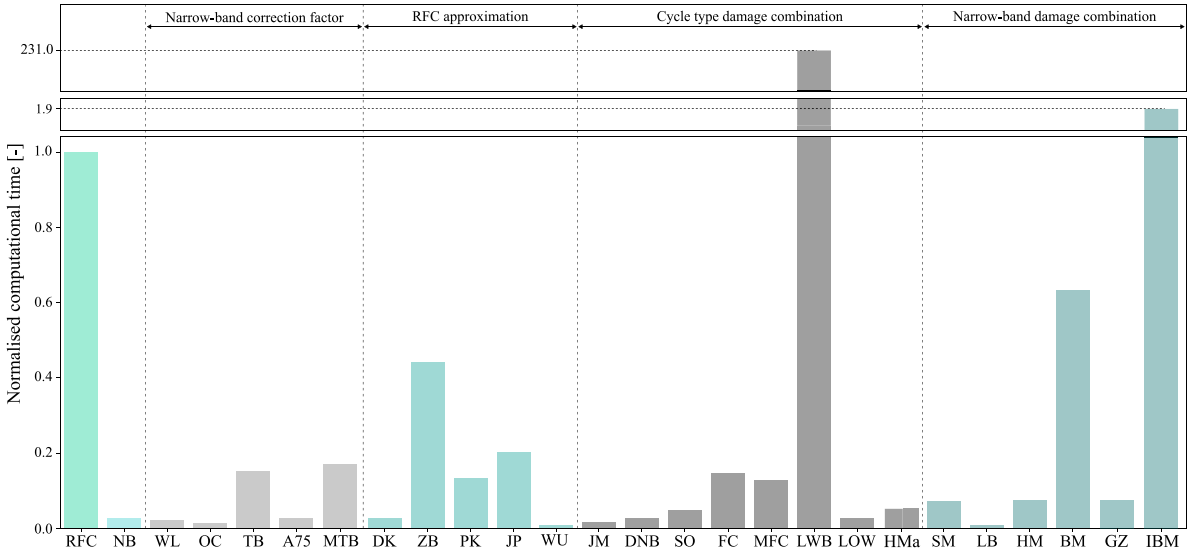

Fig. 13. Normalised computational times for each spectral method.

computational times. As for LWB, its computational burden may stem from the inherent challenge of performing two double integrals over random variables. It is crucial to note that these results are dependent on the programming abilities of the authors.

5.4. Evaluation of spectral methods

The evaluation of the selected spectral methods, as depicted in Table 7, reveals insightful observations about their performance when compared with the popularity of each method, which is measured combining the citation rate and the utilisation (*e.g., inclusion in standards or as recommended practice*). It is evident how the popularity of a method, or lack thereof, does not necessarily align with the performance level shown in this analysis. This emphasises the importance of a performance evaluation beyond the method's popularity. The NB, WL, and JM methods are clear examples of this paradox, which are highly used in the literature while showing significantly poor performance for the analysed cases, as further described in the following paragraphs.

In terms of applicability, TB stands out as the best-performing method, aligning with its popularity and showcasing an exceptional balance between simplicity and overall suitability. Its reliability positions it as the top choice for offshore fatigue analysis. Similarly, the A75 and HMa methods excel in result quality, displaying high precision and accuracy. Their main drawback lies in the non-conservative nature of the results.

The LOW method ensures high accuracy and precision, with added appeal due to its simple implementation and conservative results. The JP method demonstrates consistent reliability across every criterion, despite not being a widespread methodology. The MTB method, while not widely recognised due to its recent development, demonstrates reliable performance and straightforward implementation. On the other hand, the DK method, while showing commendable performance, is penalised for its tendency to underestimate damage. Nevertheless, it stands out for its outstanding popularity and wide acceptance in the automotive industry.

The SM method showcases good precision and accuracy, coupled with a simple formulation. However, it is essential to note that this method tends towards non-conservative values.

Furthermore, the OC, ZB, PK, WU, and DNB all earn scores above 5, indicating their overall good performance. The WU and DNB approaches, for instance, have proven their effectiveness with overall acceptable scores in all aspects, minimising the risk factor as they provide conservative results. It is important to note that for the DNB method, specific citation data was unavailable. However, a popularity score of one has been assigned because it is the recommended method in DNV (2021) and API (2005) offshore specifications, signifying its acceptance within the industry. The ZB and PK methods stand out for their ease of correct implementation, although they both exhibit non-conservative results. The GZ method provides acceptable precision and accuracy with a fast computational time; however, its attractiveness is compromised by its non-conservative nature. Despite the easy implementation and conservative results of the OC method, it is penalised for yielding numerous outliers, resulting in significantly overestimated damage values and the potential for divergent results from the overall trend of the method.

In contrast, despite their popularity, NB and WL have the lowest scores with poor result reliability, as they give very overestimated results with great dispersion. The same thing applies to FC and MFC methods. In this case, they are highly penalised for their difficult implementation as they propose formulations that require numerical integrations that cannot always be achieved (Benasciutti, 2012). On the other hand, the LWB method demonstrates remarkably good accuracy and precision, but its appeal is mitigated by the complexity of implementation and its high computational time, significantly higher than the one required by RFC.

Despite its remarkable popularity, JM performs poorly in terms of precision and especially in terms of accuracy. This method tends to be highly conservative in its estimations. A similar observation applies to the LB method, although this approach is found to be less popular.

The remaining methods fall somewhere in between, showcasing varying degrees of suitability. For example, both the HM and SO methods exhibit a relatively simple formulation, but their negative risk scores, stemming from the non-conservative nature of their results and limited accuracy, position them in a mid-range category. On the other hand, while BM and IBM demonstrate good precision and accuracy, they are penalised for non-conservative results and a longer computational time. This makes other methods more suitable for the fatigue assessment of ORE systems.

6. Conclusions

It is widely accepted that rainflow counting (RFC) in the time domain (TD) is the most accurate estimate for fatigue assessment of random loadings. However, spectral methods offer a more efficient alternative, aiming to reproduce RFC damage based on different theoretical considerations and approximation methodologies. Thus, this

Table 7
Evaluation of the selected spectral methods.

	Simple formulation	Parameter qty.	Convergence time	Computational time	Risk	Precision	Accuracy	Performance	Popularity
NB	1	1	0.25	1	0	0	0	3.25	0.75
WL	1	0.75	0.5	1	0	0	0	3.25	1
OC	1	0.5	0.25	1	0	1.5	1	5.25	0
TB	1	0.75	0.75	1	−0.25	1.63	2	6.88	1
A75	1	1	1	1	−0.5	1.75	1.5	6.75	0
MTB	1	0.75	0.75	1	−0.25	1.63	1.5	6.38	0
DK	1	0.5	0.5	1	−0.5	1.88	2	6.38	1
ZB	1	0.5	0.5	0.5	−0.25	1.63	1.5	5.38	0.75
PK	1	0.5	0.5	1	−0.5	1.63	1.5	5.63	0.75
JP	1	0.5	0.5	1	−0.25	1.63	2	6.38	0.25
WU	1	0.75	0.25	1	0	1.13	1.5	5.63	0
JM	1	0.75	0.75	1	0	0.75	0	4.25	0.75
DNB	1	0.75	0.75	1	0	1.25	1	5.75	0.25
SO	1	1	0.75	1	−0.5	1.13	0.5	4.88	0.5
FC	0	1	0.75	1	0	0.75	0.5	4	0
MFC	0	1	0.75	1	0	0.38	0.5	3.63	0.5
LWB	0.25	0.5	0.5	0	−0.5	1.75	2	4.5	0.25
LOW	1	0.75	0.5	1	0	1.75	1.5	6.5	1
HMa	1	1	0.5	1	−0.5	1.63	2	6.63	0.5
SM	1	1	0.75	1	−0.5	1.63	1	5.88	0.5
LB	1	0.75	0.75	1	0	0.38	0	3.88	0.25
HM	1	0.75	1	1	−0.5	0.75	0.5	4.5	0.25
BM	0.75	0.75	0.75	0.25	−0.5	1.63	1	4.63	1
GZ	0.75	0.75	1	1	−0.5	1.63	1	5.63	0.5
IBM	0.75	0.5	0.75	0	−0.5	1.63	1	4.13	0.75
Max.	1	1	1	1	0	2	2	8	1

study evaluates different spectral methods for fatigue analysis, using RFC as a reference method. The research focuses on offshore renewable energy (ORE) applications and, more specifically, mooring lines, considering their distinct features and requirements.

First, synthetic signals that effectively mimic realistic loads were designed. These signals incorporate bimodal components, representing both low-frequency and wave-frequency characteristics. This approach successfully captures the intricate conditions of ORE applications, enabling the assessment of a total of 70 sea states, each of which is represented by 50 realisations. Based on these synthetic signals, 20 different spectral methods were assessed.

In summary, the conducted benchmarking analysis provides valuable insights into the suitability of spectral methods for fatigue assessment in offshore applications, with a few methods exhibiting potential for accurate fatigue assessment.

The RFC PDF approximation stands out as the most consistently effective. This approach assumes that the RFC distribution can be obtained from a blend of well-known probability distributions, which are then adjusted using simulation data. Consequently, adhering to this method seems to guarantee a higher success rate compared to relying on theoretical assumptions that might lack precision and reliability.

However, the spectral method that presents the best overall performance in this case study is the Tovo–Benasciutti (TB) method, which belongs to the narrow-band correction factor approach. The estimations obtained with the TB method display a mean damage difference of 4% and a result dispersion of 2%, closely mirroring the RFC damage calculation.

In addition to the highlighted findings, the benchmarking study revealed several noteworthy conclusions, outlined briefly below:

- The empirical $\alpha_{0.75}$, Han–Ma, Low, Modified Tovo–Benasciutti, Jun–Park, Dirlik, and Single Moment techniques also provide suitable damage estimations.
- Despite being tailored for bimodal loads typical in ORE settings, the Jiao–Moan (JM) method yielded unsatisfactory results in this study. Moreover, the impact of the bandwidth parameter is significant. This underscores the crucial role of meticulous parameter selection and its impact on the accuracy of fatigue assessment.
- The outcomes for the Narrow-band method suggest that assuming ORE loads follow a narrow-band distribution might be insufficient. This highlights the importance of considering broader frequency ranges and more intricate load characteristics in fatigue assessments for offshore structures.
- Lastly, the evaluation of the Wirsching Light (WL) method reveals notable deficiencies in accuracy despite its popularity, with a mean damage difference of 32% and a lack of precision, showing a dispersion of 33%.

The recorded computational times for each method indicate that almost all spectral methods, with the exception of Low's Bimodal and Improved Bands methods, significantly reduce the time needed for fatigue assessment relative to the time needed via RFC. This observation aligns with claims in the existing literature, underscoring the advantageous role of spectral methods in efficiently addressing fatigue assessment for ORE systems, particularly when dealing with a large number of variable loading conditions.

Last but not least, mean stress is ignored in the vast majority of methods and ORE applications in the literature. However, in general fatigue studies, it is commonly addressed because its presence can influence fatigue life.

It is important to emphasise that, as different stress responses possess different spectral characteristics, the specific ranking established for the specific analysis of mooring lines in ORE structures may not be suitable for other applications. Nevertheless, the overall systematic methodology presented in this benchmarking study may be followed to assess the suitability of various spectral methods for responses with different characteristics.

To conclude, the codes used for the benchmarking study, including all the TD and spectral approaches, have been released in open-source and are available at https://github.com/MGEP-Fluidos/ORE-Structural-Integrity.git.

CRediT authorship contribution statement

Eguzkiñe Martinez-Puente: Writing – original draft, Visualization, Validation, Software, Methodology, Data curation, Conceptualization.

Ander Zarketa-Astigarraga: Writing – review & editing, Software, Data curation. **Manex Martinez-Agirre:** Writing – review & editing, Data curation, Conceptualization. **Alaitz Zabala:** Writing – review & editing, Methodology, Conceptualization. **Jon Ander Esnaola:** Writing – review & editing, Methodology, Conceptualization. **Miguel Muñiz-Calvente:** Writing – review & editing, Methodology, Conceptualization. **Iñigo Llavori:** Writing – review & editing, Supervision, Software, Funding acquisition, Data curation, Conceptualization. **Markel Penalba:** Writing – review & editing, Visualization, Supervision, Methodology, Funding acquisition, Data curation, Conceptualization.

Declaration of competing interest

The authors declare that they have no known competing financial interests or personal relationships that could have appeared to influence the work reported in this paper.

Data availability

The codes used for the benchmarking study have been released in open-source and are available at https://github.com/MGEP-Fluidos/ORE-Structural-Integrity.git.

Declaration of Generative AI and AI-assisted technologies in the writing process

During the preparation of this work the authors used GPT3.5 in order to improve readability and language. After using this tool, the authors reviewed and edited the content as needed and take full responsibility for the content of the publication.

Acknowledgements

This publication is part of the research project PID2021-124245OA-I00 funded by MCIN/AEI/10.13039/501100011033 and by ERDF A way of making Europe, and further supported by the Basque Government under the Project STEINER Grant No. PIBA_2023_1_0052. In addition, the authors from the Fluid Mechanics research group at Mondragon University are also supported by the Basque Government's Research Group Program under the grant No. IT1505-22.

References

API, R., 2005. 2SK. Recommended practice for design and analysis of stationkeeping systems for floating structures.

Astariz, S., Iglesias, G., 2015. The economics of wave energy: A review. Renew. Sustain. Energy Rev. 45, 397–408.

Barrera, C., Battistella, T., Guanche, R., Losada, I.J., 2020. Mooring system fatigue analysis of a floating offshore wind turbine. Ocean Eng. 195, 106670.

Benasciutti, D., 2012. Fatigue Analysis of Random Loadings. A Frequency-Domain Approach. LAP Lambert Academic Publishing AG & Co KG.

Benasciutti, D., Cristofori, A., Tovo, R., 2013. Analogies between spectral methods and multiaxial criteria in fatigue damage evaluation. Probab. Eng. Mech. 31, 39–45.

Benasciutti, D., Tovo, R., 2004. Rainflow Cycle Distribution and Fatigue Damage in Gaussian Random Loadings. Report of engineering department. University of Ferrara (Italy).

Benasciutti, D., Tovo, R., 2005. Spectral methods for lifetime prediction under wide-band stationary random processes. Int. J. Fatigue 27 (8), 867–877. http://dx.doi.org/10.1016/j.ijfatigue.2004.10.007, Cumulative Fatigue Damage Conference - University of Seville 2003.

Benasciutti, D., Tovo, R., 2007. On fatigue damage assessment in bimodal random processes. Int. J. Fatigue 29 (2), 232–244. http://dx.doi.org/10.1016/j.ijfatigue.2006.03.013.

Benites-Munoz, D., Ricci, P., Touzon, I., Salcedo, F., Raymond, R., Nunes, D., 2023. Fatigue-life prediction methods of a dynamic power cable for a floating testing platform–a numerical approach. In: Proceedings of the European Wave and Tidal Energy Conference, Vol. 15.

Bergara, A., Arredondo, A., Altuzarra, J., Martínez-Esnaola, J.M., 2022. Fatigue crack propagation analysis in offshore mooring chains and the influence of manufacturing residual stresses. Ocean Eng. 257, 111605.

Braccesi, C., Cianetti, F., Tomassini, L., 2015. Random fatigue. a new frequency domain criterion for the damage evaluation of mechanical components. Int. J. Fatigue 70, 417–427. http://dx.doi.org/10.1016/j.ijfatigue.2014.07.005.

Catapult, O., 2023. Wind farm costs | Guide to a floating offshore wind farm. URL https://guidetofloatingoffshorewind.com/wind-farm-costs/.

Cevasco, D., Collu, M., Rizzo, C., Hall, M., 2018. On mooring line tension and fatigue prediction for offshore vertical axis wind turbines: a comparison of lumped mass and quasi-static approaches. Wind Eng. 42 (2), 97–107.

Cortabitarte, G., Llavori, I., Esnaola, J., Blasón, S., Larrañaga, M., Larrañaga, J., Arana, A., Ulacia, I., 2023. Application of the theory of critical distances for fatigue life assessment of spur gears. Theor. Appl. Fract. Mech. 128, 104086. http://dx.doi.org/10.1016/j.tafmec.2023.104086.

Couñago Lorenzo, B., Barturen Antépara, R., Díaz Huerta, I., 2010. Estudio técnico-financiero sobre la construcción de un parque eólico marino flotante en el litoral español. Ingeniería naval 79 (886), 85–105.

Davidson, J., Ringwood, J.V., 2017. Mathematical modelling of mooring systems for wave energy converters—A review. Energies 10 (5), 666.

Dinmohammadi, F., Flynn, D., Bailey, C., Pecht, M., Yin, C., Rajaguru, P., Robu, V., 2019. Predicting damage and life expectancy of subsea power cables in offshore renewable energy applications. IEEE Access 7, 54658–54669.

Dirlik, T., 1985. Application of Computers in Fatigue Analysis (Ph.D. thesis). University of Warwick, URL http://webcat.warwick.ac.uk/record=b1445503~S9.

DNV, G., 2021. Offshore standard-position mooring (DNVGL-OS-e301). Edition July.

Durodola, J., Li, N., Ramachandra, S., Thite, A., 2017. A pattern recognition artificial neural network method for random fatigue loading life prediction. Int. J. Fatigue 99, 55–67.

Farley, F., 2013. Capture width for arrays of wave energy converters. Energy and Climate Change Division, University of Southampton. Available online: http://www.iwwwfb.org/Abstracts/iwwwfb28/iwwwfb28_18.pdf. (Accessed on 1 December 2012).

Fu, T.T., Cebon, D., 2000. Predicting fatigue lives for bi-modal stress spectral densities. Int. J. Fatigue 22 (1), 11–21. http://dx.doi.org/10.1016/S0142-1123(99)00113-9.

Gao, Z., Moan, T., 2008. Frequency-domain fatigue analysis of wide-band stationary Gaussian processes using a trimodal spectral formulation. Int. J. Fatigue 30 (10), 1944–1955. http://dx.doi.org/10.1016/j.ijfatigue.2008.01.008.

Gao, Z., Moan, T., 2009. Mooring system analysis of multiple wave energy converters in a farm configuration. In: Proceedings of the 8th European Wave and Tidal Energy Conference. Uppsala, Sweden, pp. 7–10.

Gao, S., Zheng, X.Y., 2019. An improved spectral discretization method for fatigue damage assessment of bimodal Gaussian processes. Int. J. Fatigue 119, 268–280.

Giro, F., Mishael, J., Morato, P.G., Rigo, P., 2022. Inspection and maintenance planning for offshore wind support structures: Modelling reliability and inspection costs at the system level. In: International Conference on Offshore Mechanics and Arctic Engineering, vol. 85864, American Society of Mechanical Engineers, V002T02A065.

Gondal, I.A., 2019. Offshore renewable energy resources and their potential in a green hydrogen supply chain through power-to-gas. Sustain. Energy Fuels 3 (6), 1468–1489.

Goodman, J., 1919. Mechanics Applied to Engineering. Longmans, Green.

Han, C., Ma, Y., Qu, X., Yang, M., Qin, P., 2016. A practical method for combination of fatigue damage subjected to low–frequency and high–frequency Gaussian random processes. Appl. Ocean Res. 60, 47–60.

Harris, R.E., Johanning, L., Wolfram, J., 2004. Mooring systems for wave energy converters: A review of design issues and choices. Marec2004 180–189.

Hasselmann, K., Barnett, T.P., Bouws, E., Carlson, H., Cartwright, D.E., Enke, K., Ewing, J., Gienapp, A., Hasselmann, D., Kruseman, P., et al., 1973. Measurements of wind-wave growth and swell decay during the joint north sea wave project (JONSWAP). Ergaenzungsheft zur Deutschen Hydrographischen Zeitschrift, Reihe A.

He, W., Cao, S., Hu, Z., Xie, D., Zhang, Z., Wang, C., 2022. Numerical evaluation on fatigue crack growth and life predictions of an FPSO mooring system. Ocean Eng. 265, 112501.

Huang, W., Moan, T., 2006. Fatigue under combined high and low frequency loads. In: International Conference on Offshore Mechanics and Arctic Engineering, Volume 3: Safety and Reliability; Materials Technology; Douglas Faulkner Symposium on Reliability and Ultimate Strength of Marine Structures, pp. 149–156. http://dx.doi.org/10.1115/OMAE2006-92247.

IRENA, E., 2020. Innovation Outlook: Ocean Energy Technologies. International Renewable Energy Agency Abu Dhabi, United Arab Emirates.

IRENA, S., 2021. Offshore Renewables: An Action Agenda for Deployment. International Renewable Energy Agency Abu Dhabi, United Arab Emirates.

Jiao, G., Moan, T., 1990. Probabilistic analysis of fatigue due to Gaussian load processes. Probab. Eng. Mech. 5 (2), 76–83. http://dx.doi.org/10.1016/0266-8920(90)90010-H.

Jun, S.H., Park, J.B., 2020. Development of a novel fatigue damage model for Gaussian wide band stress responses using numerical approximation methods. Int. J. Naval Archit. Ocean Eng. 12, 755–767. http://dx.doi.org/10.1016/j.ijnaoe.2020.09.005.

Larsen, C., Lutes, L., 1991. Predicting the fatigue life of offshore structures by the single-moment spectral method. Probab. Eng. Mech. 6 (2), 96–108. http://dx.doi.org/10.1016/0266-8920(91)90023-W.

Lee, G.N., Ngo, D.V., Lee, S.I., Kim, D.H., 2023. Fatigue life convergence of offshore wind turbine support structure according to wind measurement period. Energies 16 (7), 3199.

Lee, Y.L., Tjhung, T., 2012. Chapter 3 - Rainflow cycle counting techniques. In: Lee, Y.L., Barkey, M.E., Kang, H.T. (Eds.), Metal Fatigue Analysis Handbook. Butterworth-Heinemann, pp. 89–114. http://dx.doi.org/10.1016/B978-0-12-385204-5.00003-3.

Leijon, M., Danielsson, O., Eriksson, M., Thorburn, K., Bernhoff, H., Isberg, J., Sundberg, J., Ivanova, I., Sjöstedt, E., Ågren, O., et al., 2006. An electrical approach to wave energy conversion. Renew. Energy 31 (9), 1309–1319.

Li, C.B., Choung, J., Noh, M.H., 2018. Wide-banded fatigue damage evaluation of catenary mooring lines using various artificial neural networks models. Mar. Struct. 60, 186–200.

Llavori, I., Zabala, A., Aginagalde, A., Tato, W., Ayerdi, J., Gómez, X., 2020. Critical analysis of coefficient of friction derivation methods for fretting under gross slip regime. Tribol. Int. 143, 105988.

Lotsberg, I., 2005. Background for revision of DNV-RP-C203 fatigue analysis of offshore steel structure. In: International Conference on Offshore Mechanics and Arctic Engineering, vol. 41979, pp. 297–306. http://dx.doi.org/10.1115/OMAE2005-67549.

Low, Y., 2010. A method for accurate estimation of the fatigue damage induced by bimodal processes. Probab. Eng. Mech. 25 (1), 75–85. http://dx.doi.org/10.1016/j.probengmech.2009.08.001.

Low, Y., 2014. A simple surrogate model for the rainflow fatigue damage arising from processes with bimodal spectra. Mar. Struct. 38, 72–88. http://dx.doi.org/10.1016/j.marstruc.2014.06.005.

Lutes, L.D., Corazao, M., Hu, S.L.J., Zimmerman, J., 1984. Stochastic fatigue damage accumulation. J. Struct. Eng. (United States) 110 (11), 2585–2601. http://dx.doi.org/10.1061/(ASCE)0733-9445(1984)110:11(2585), Cited by: 109.

Lutes, L.D., Larsen, C.E., 1990. Improved spectral method for variable amplitude fatigue prediction. J. Struct. Eng. (United States) 116 (4), 1149–1164. http://dx.doi.org/10.1061/(ASCE)0733-9445(1990)116:4(1149), Cited by: 109.

Ma, K.T., Luo, Y., Kwan, T., Wu, Y., 2019a. Chapter 6 - Fatigue analysis. In: Ma, K.T., Luo, Y., Kwan, T., Wu, Y. (Eds.), Mooring System Engineering for Offshore Structures. Gulf Professional Publishing, pp. 115–137. http://dx.doi.org/10.1016/B978-0-12-818551-3.00006-5.

Ma, K.T., Luo, Y., Kwan, T., Wu, Y., 2019b. Chapter 9 - Hardware—off-vessel components. In: Ma, K.T., Luo, Y., Kwan, T., Wu, Y. (Eds.), Mooring System Engineering for Offshore Structures. Gulf Professional Publishing, pp. 175–198. http://dx.doi.org/10.1016/B978-0-12-818551-3.00009-0.

Madsen, H.O., Krenk, S., Lind, N.C., 2006. Methods of Structural Safety. Courier Corporation.

Martinez, A., Iglesias, G., 2022. Mapping of the levelised cost of energy for floating offshore wind in the European Atlantic. Renew. Sustain. Energy Rev. 154, 111889.

Matsuishi, M., Endo, T., 1968. Fatigue of metals subjected to varying stress. Japan Soc. Mech. Eng. Fukuoka, Japan 68 (2), 37–40.

Miles, J.W., 1954. On structural fatigue under random loading. J. Aeronaut. Sci. 21 (11), 753–762. http://dx.doi.org/10.2514/8.3199.

Miner, M.A., 1945. Cumulative damage in fatigue. J. Appl. Mech. http://dx.doi.org/10.1115/1.4009458.

Muñiz-Calvente, M., Álvarez-Vázquez, A., Pelayo, F., Aenlle, M., García-Fernández, N., Lamela-Rey, M., 2022. A comparative review of time- and frequency-domain methods for fatigue damage assessment. Int. J. Fatigue 163, 107069. http://dx.doi.org/10.1016/j.ijfatigue.2022.107069.

Neary, V., Previsic, M., Jepsen, R., Lawson, M., Yu, Y., Copping, A., Fontaine, A., Hallett, K., Murray, D., 2014. Reference model project (RMP) : Sandia energy. URL https://energy.sandia.gov/programs/renewable-energy/water-power/projects/reference-model-project-rmp/.

Nesládek, M., Pacetti, L., Papuga, J., 2022. Validation of fatigue criteria under fretting fatigue conditions. Int. J. Fatigue 161, 106895.

NREL and Sandia, 2022. WEC-Sim (Wave energy converter SIMulator) — WEC-Sim documentation. URL http://wec-sim.github.io/WEC-Sim/master/index.html.

Okpokparoro, S., Sriramula, S., 2023. Reliability analysis of floating wind turbine dynamic cables under realistic environmental loads. Ocean Eng. 278, 114594.

Ortiz, K., Chen, N., 1987. Fatigue damage prediction for stationary wideband processes. In: Proc. Fifth Int. Conf. on Applications of Statistics and Probability in Soil and Struct. Engrg.

Park, J.B., Choung, J., Kim, K.S., 2014. A new fatigue prediction model for marine structures subject to wide band stress process. Ocean Eng. 76, 144–151. http://dx.doi.org/10.1016/j.oceaneng.2013.11.002.

Penalba, M., Aizpurua, J.I., Martinez-Perurena, A., 2021. On the definition of a risk index based on long-term metocean data to assist in the design of Marine Renewable Energy systems. Ocean Eng. 242, 110080. http://dx.doi.org/10.1016/j.oceaneng.2021.110080.

Petrucci, G., Zuccarello, B., 2004. Fatigue life prediction under wide band random loading. Fatigue Fract. Eng. Mater. Struct. 27 (12), 1183–1195.

Pham, H.D., Schoefs, F., Cartraud, P., Soulard, T., Pham, H.H., Berhault, C., 2019. Methodology for modeling and service life monitoring of mooring lines of floating wind turbines. Ocean Eng. 193, 106603.

Poon, C.T., Mullins, C., Radziunas, L., O'Connell, E., Connolly, A., Leen, S., 2022. Finite element design study of dynamics in submarine power cables for offshore renewable wind energy. In: International Conference on Offshore Mechanics and Arctic Engineering, vol. 86618, American Society of Mechanical Engineers, V001T01A023.

Previsic, M., Chozas, J., 2015. International Levelised Cost of Energy for Ocean Energy Technologies. http://dx.doi.org/10.13140/RG.2.2.34304.38407.

Rychlik, I., 1993. On the 'narrow-band' approximation for expected fatigue damage. Probab. Eng. Mech. 8 (1), 1–4. http://dx.doi.org/10.1016/0266-8920(93)90024-P.

Sakai, S., Okamura, H., 1995. On the distribution of rainflow range for Gaussian random processes with bimodal PSD. JSME Int. J. Ser. A, Mech. Mater. Eng. 38 (4), 440–445. http://dx.doi.org/10.1299/jsmea1993.38.4_440.

Schnepf, A., Giljarhus, K.E.T., Johnsen, Ø., Lopez-Pavon, C., 2023. Dynamic power cable configuration design for floating offshore wind turbines using gradient-based optimization. In: International Conference on Offshore Mechanics and Arctic Engineering, vol. 86908, American Society of Mechanical Engineers, V008T09A037.

Shahroozi, Z., Göteman, M., Engström, J., 2022. Fatigue analysis of a point-absorber wave energy converter based on augmented data from a WEC-sim model calibrated with experimental data. Trends Renew. Energies Offshore 925–933.

Slavič, J., Boltezar, M., Mrsnik, M., Cesnik, M., Javh, J., 2020. Vibration Fatigue by Spectral Methods: From Structural Dynamics to Fatigue Damage – Theory and Experiments. Elsevier, http://dx.doi.org/10.1016/C2019-0-04580-3.

Sobhaniasl, M., Petrini, F., Karimirad, M., Bontempi, F., 2020. Fatigue life assessment for power cables in floating offshore wind turbines. Energies 13 (12), 3096.

Sykes, V., Collu, M., Coraddu, A., 2023. A review and analysis of optimisation techniques applied to floating offshore wind platforms. Ocean Eng. 285, 115247.

Tovo, R., 2002. Cycle distribution and fatigue damage under broad-band random loading. Int. J. Fatigue 24 (11), 1137–1147. http://dx.doi.org/10.1016/S0142-1123(02)00032-4.

Vanmarcke, E.H., 1972. Properties of spectral moments with applications to random vibration. J. Eng. Mech. Div. 98 (2), 425–446. http://dx.doi.org/10.1061/JMCEA3.0001593.

Wirsching, P.H., Light, M.C., 1980. Fatigue under wide band random stresses. J. Struct. Div. 106 (7), 1593–1607. http://dx.doi.org/10.1061/JSDEAG.0005477.

Wu, B., Lu, W., Li, X., Kou, Y., Wei, Q., Guo, X., 2023. A new frequency-domain method for fatigue prediction of offshore structures under wideband random loadings. Ocean Eng. 281, 114812.

Xu, S., Soares, C.G., 2021. Evaluation of spectral methods for long term fatigue damage analysis of synthetic fibre mooring ropes based on experimental data. Ocean Eng. 226, 108842.

Yuan, K., Jin, H., Chai, W., 2023. Development of a new spectral method for fatigue damage assessment in bimodal and trimodal Gaussian random processes. Ocean Eng. 267, 113273.

Yuan, K., Sun, Z., 2023. A spectral method for accurate evaluation of fatigue damage induced by wide-band non-Gaussian random processes. Ocean Eng. 281, 115002.

Zhao, W., Baker, M.J., 1992. On the probability density function of rainflow stress range for stationary Gaussian processes. Int. J. Fatigue 14 (2), 121–135. http://dx.doi.org/10.1016/0142-1123(92)90088-T.

Zhao, S., Cheng, Y., Chen, P., Nie, Y., Fan, K., 2021. A comparison of two dynamic power cable configurations for a floating offshore wind turbine in shallow water. AIP Adv. 11 (3).

Zhao, Y., Dong, S., 2021. Probabilistic fatigue surrogate model of bimodal tension process for a semi-submersible platform. Ocean Eng. 220, 108501.

Zhao, G., Zhao, Y., Dong, S., 2023. System reliability analysis of mooring system for floating offshore wind turbine based on environmental contour approach. Ocean Eng. 285, 115157.

Zorman, A., Slavič, J., Boltežar, M., 2023. Vibration fatigue by spectral methods—A review with open-source support. Mech. Syst. Signal Process. 190, 110149. http://dx.doi.org/10.1016/j.ymssp.2023.110149.